

An Efficient Shock-Capturing Algorithm for Compressible Multicomponent Problems

Keh-Ming Shyue

Department of Mathematics, National Taiwan University, Taipei, Taiwan, Republic of China

E-mail: shyue@math.ntu.edu.tw

Received January 6, 1997; revised January 22, 1998

A simple shock-capturing approach to multicomponent flow problems is developed for the compressible Euler equations with a stiffened gas equation of state in multiple space dimensions. The algorithm uses a quasi-conservative formulation of the equations that is derived to ensure the correct fluid mixing when approximating the equations numerically with interfaces. A γ -based model and a volume-fraction model have been described, and both of them are solved using the standard high-resolution wave propagation method for general hyperbolic systems of partial differential equations. Several calculations are presented with a Roe approximate Riemann solver that show accurate results obtained using the method without any spurious oscillations in the pressure near the interfaces. Convergence of the computed solutions to the correct weak ones has been verified for a two-dimensional Richtmyer–Meshkov unstable interface problem where we have performed a mesh-refinement study and also shown front-tracking results for comparison. © 1998 Academic Press

1. INTRODUCTION

Our goal is to present a simple approach to multicomponent flow of general compressible materials in more than one dimension. We use the Euler equations of gas dynamics as a model system, and consider problems with the so-called “stiffened” gas equation of state for approximating materials including compressible liquids and solids [29, 50]. The algorithm uses a quasi-conservative formulation of the equations proposed by Abgrall [1] to ensure a consistent approximation of the energy equation near the interfaces where regions of different fluid components are separated. A γ -based model is therefore derived that extends the work of Abgrall [1] from polytropic gases in one dimension to a stiffened gas, and also to multiple dimensions. We give a new formulation of the resulting model in expression of the volume fraction that is more robust for two-component flow problems. This will be discussed further in Sections 2 and 5.

We use the high-resolution wave propagation method developed by LeVeque [40, 41, 43] to solve the proposed multicomponent models. This method is a variant of the *fluctuation-and-signal* method of Roe [59, 60], and has been widely used in many applications including the single-component fluid of ideal gases. The main idea behind the method has recently been implemented in the software package CLAWPACK (Conservation LAWs PACKage) as the underlying integration routine [46, 47]. The current use of the method is just an easy extension of the previous one from single-component to multicomponent problems. It is an efficient and yet accurate scheme without any spurious oscillations in the pressure near an interface as illustrated by numerical results presented in this paper.

We will only briefly review and describe the method in a shock-capturing framework in one dimension, see Section 3. Extensions of the method to front-tracking and to two dimensions are straightforward also by following the procedures outlined in [44, 45], for example. We will not discuss a front-tracking version of the method here, but focus on the more fundamental shock-capturing algorithm and validate its use *via* numerical experimentations. Some preliminary results obtained using the front tracking method may be found in [65, 66] for two-dimensional unstable fluid interface problems such as Rayleigh–Taylor and Richtmyer–Meshkov instabilities, see Section 6 for an example also. Generalization of the approach to three dimensions can be made in a similar manner, but requires more programming work, especially in regard to a front-tracking method [25].

Clearly for real applications the use of a stiffened gas equation of state that appears in an analytical formula (i.e., the constitutive relation (2) in Section 2) represents only a limited number of materials of practical importance [29, 50]. However, there are some problems of sufficient interest and difficulty that the development of a multicomponent algorithm for this equation of state is worthwhile, particularly since in some cases it is relatively easy to compute the exact solutions and check accuracy of the method.

Numerous numerical methods have been developed over the years to handle multicomponent flow problems. Consider a non-reacting ideal gas flow, for example. One popular approach among them is to solve an extended system of equations in which additional conservation equations are introduced to the original Euler equations to describe the conservation of each fluid component separately. Methods of this type, in particular a shock-capturing version of the method, often fail to maintain pressure equilibrium for grid cells near interfaces where two or more fluid components are mixed. Some representative examples that exhibit this erroneous phenomenon are given in [34] for the use of a γ -based (see Fig. 1 also) and a level-set model, and in [9, 12, 71] for the use of a mass-fraction model. The exception is the method explained by Jenny *et al.* [33] that the fluxes obtained using conservative Euler solvers are modified in a suitable way to avoid the occurrence of the pressure errors generated near the interfaces. It is unclear how to extend the method to a situation other than the ideal gas flows, however.

Another approach introduced by Karni [35, 36] is to solve the Euler equations separately on each side of the interface using a method designed for a single-component flow, while the interface is dealt with in a different manner using a pressure evolution equation derived from the energy equation. Despite the fact that the method is not exactly conservative at the interface, reasonable results are obtained using this approach in conjunction with either standard level-set or mass-fraction formulation of ideal gases. Extension of the method to a thermally perfect gas was done recently by Fedkiw *et al.* [21] in one dimension. It should be noted that Cocchi *et al.* [12] devised a rather similar method of this kind that employs a

linear interpolation technique near the interface instead; some one-dimensional results are shown for a stiffened gas flow.

Our method to modeling multicomponent flow of general compressible materials is motivated by the work of Abgrall [1] in that, based on the physical principles and from the energy equation, we derive the effective equations (see Section 2) for the mixture of material-dependent quantities near the interface. In this method, with the stiffened gas equation of state, we take these equations to be of the form that do not vary their solutions across the shock and rarefaction waves as well. Combining the resulting effective equations (i.e., Eqs. (9)) to the Euler equations yields a model system that is not written in the full conservation form, but is rather a quasi-conservative system of equations. Abgrall [1] solves a system of this kind using a predictor-corrector method, while we use the high-resolution wave propagation method that gives an efficient implementation of the algorithm. In principle, when properly modified, it is possible to employ the state-of-the-art shock-capturing methods for hyperbolic systems of conservation laws for solving the model equations as well; see [67] for an example that generalizes the MUSCL scheme [13, 72] to this specific application and also to a van der Waals gas.

There are many other multicomponent approaches available in the literature. Some typical ones are the level-set methods [19, 52], front-tracking methods [25, 28], volume-of-fluid methods [14, 51, 55, 71], and the BGK-based method [74].

This paper is organized as follows. In Section 2, we begin by discussing the basic computational models in one dimension that govern the motion of materials characterized by a stiffened gas equation of state in a multicomponent environment. We will give two different formulations of the model equations that are both applicable for practical computations of multicomponent problems. In Section 3, we briefly review an approximate Riemann solver of Roe, and analyze a first order numerical methods based on a wave-propagation approach with an application to our multicomponent models proposed in Section 2. The results of some one-dimensional tests are given in Section 4 that validate this approach. The basic idea of the algorithm is then extended to multiple dimensions in Section 5, and some two-dimensional numerical results are presented. Section 6 shows results for a Richtmyer–Meshkov unstable interface problem where a mesh-refinement study is performed to check convergence of the computed solutions.

2. DERIVATION OF MODEL EQUATIONS

In one dimension, the single-component Euler equations of gas dynamics take the form

$$\frac{\partial}{\partial t} \begin{pmatrix} \rho \\ \rho u \\ \rho E \end{pmatrix} + \frac{\partial}{\partial x} \begin{pmatrix} \rho u \\ \rho u^2 + p \\ (\rho E + p)u \end{pmatrix} = 0, \quad (1)$$

where ρ is the density, u is the velocity, p is the pressure, and E is the total energy per unit mass. We assume a compressible material that the internal energy per unit mass, denoted by e , satisfies the “stiffened” gas equation of state,

$$\rho e = \frac{p + \gamma p_\infty}{\gamma - 1}, \quad (2)$$

and $E = e + u^2/2$. Here γ is the usual ratio of specific heats ($\gamma > 1$), and p_∞ is a prescribed pressure-like constant; these values can be used to describe the material property of interests and can be determined from laboratory experiments *via* an empirical fit [31, 49]. For example, for water we have $\gamma \cong 5.5$, $p_\infty = 4921.15$ bars [12], and for tungsten we get $\gamma \cong 3.14$, $p_\infty = 1.0$ Mbar [54]. Note a stiffened gas reduces to a polytropic gas when $p_\infty = 0$. The three components of Eqs. (1) express the conservation of mass, momentum, and energy, respectively [18].

We are interested in the simulation of multicomponent flow problems. For the equations, we take a popular approach by considering the Euler Eqs. (1) as a model system, see [33, 74] for the use of other governing equations. Our goal here is to derive computational models that may prevent pressure oscillations near the interfaces, when solving the problem numerically with standard shock-capturing methods.

2.1. Preliminary. To begin, suppose that there are m different fluid components in a grid cell, and each of them occupies a distinct region with a volume-fraction function $Y^{(i)}$ in relation to it, for $i = 1, 2, \dots, m$. Here by the standard assumptions we have $Y^{(i)} \in [0, 1]$ and $\sum_{i=1}^m Y^{(i)} = 1$. Suppose that for each component i the state variables such as $\rho^{(i)}$, $u^{(i)}$, $p^{(i)}$, $\gamma^{(i)}$, and $p_\infty^{(i)}$ are known a priori. The objective is to define the mixture of the pressure p as well as the conserved variables ρ , ρu , and ρE in a consistent manner within the cell for the Euler Eqs. (1). Note this step is necessary when we initialize the data for computations.

To accomplish this, we follow a common practice by setting ρ , ρu , and ρE as a volume-weighted sum over the set of components $\rho^{(i)}$, $\rho^{(i)}u^{(i)}$, and $\rho^{(i)}E^{(i)}$, for each separately,

$$\rho = \sum_{i=1}^m Y^{(i)} \rho^{(i)}, \quad \rho u = \sum_{i=1}^m Y^{(i)} \rho^{(i)} u^{(i)}, \quad \rho E = \sum_{i=1}^m Y^{(i)} \rho^{(i)} e^{(i)} + \frac{1}{2} \sum_{i=1}^m Y^{(i)} \rho^{(i)} u^{(i)2}, \quad (3)$$

where u is the velocity mixture that can be computed easily by

$$u = \frac{\rho u}{\rho} = \frac{\sum_{i=1}^m Y^{(i)} \rho^{(i)} u^{(i)}}{\sum_{i=1}^m Y^{(i)} \rho^{(i)}}.$$

To find the pressure mixture p , we need to use the equation of state (2). From (3), after some simple algebra, we find

$$\frac{p + \gamma p_\infty}{\gamma - 1} = \rho e = \sum_{i=1}^m Y^{(i)} \rho^{(i)} e^{(i)} = \sum_{i=1}^m Y^{(i)} \left(\frac{p^{(i)} + \gamma^{(i)} p_\infty^{(i)}}{\gamma^{(i)} - 1} \right). \quad (4)$$

Note this gives us one equation that is not only for the mixture of p but also for γ and p_∞ . Obviously, we need to choose two supplementary conditions so as to have p , γ , and p_∞ defined well, leading to the full agreement of (4).

The basic idea of our approach is quite simple. We first split (4) into two parts by setting the terms

$$\frac{p}{\gamma - 1} = \sum_{i=1}^m \frac{Y^{(i)} p^{(i)}}{\gamma^{(i)} - 1} \quad \text{and} \quad \frac{\gamma p_\infty}{\gamma - 1} = \sum_{i=1}^m \frac{Y^{(i)} \gamma^{(i)} p_\infty^{(i)}}{\gamma^{(i)} - 1}; \quad (5)$$

this provides us with one condition right away. We then impose the following condition to the computation of γ ,

$$\frac{1}{\gamma - 1} = \sum_{i=1}^m \frac{Y^{(i)}}{\gamma^{(i)} - 1}. \quad (6a)$$

Clearly when γ is known, from (5), it is an easy matter to determine the unknowns p and p_∞ . The results are

$$p = \left(\sum_{i=1}^m \frac{Y^{(i)} p^{(i)}}{\gamma^{(i)} - 1} \right) / \left(\sum_{i=1}^m \frac{Y^{(i)}}{\gamma^{(i)} - 1} \right) \quad (6b)$$

and

$$p_\infty = \left(\sum_{i=1}^m \frac{Y^{(i)} \gamma^{(i)} p_\infty^{(i)}}{\gamma^{(i)} - 1} \right) / \left(1 + \sum_{i=1}^m \frac{Y^{(i)}}{\gamma^{(i)} - 1} \right). \quad (6c)$$

Notice that in case each of the partial pressures $p^{(i)}$ is in equilibrium within a grid cell the pressure p acquired from (6b) would remain in equilibrium also, i.e., $p = p^{(i)}$, for $i = 1, 2, \dots, m$. This nice property on the mixture of p is in fact the main reason why we use (6a), but not other ways to compute γ , see [14, 55] for a more rigorous derivation. In addition, we get the total pressure $p = \sum_{i=1}^m Y^{(i)} p^{(i)}$ when the grid cell is composed of the same set of $\gamma^{(i)}$ but with different $p^{(i)}$. We use (6c) for the mixture of p_∞ in order to make sure that (4) is handled in a consistent manner.

It is worthwhile to mention that in case $Y^{(i)}$ represents a mass-fraction function of the i th component with $\rho^{(i)} = \rho Y^{(i)}$, we would have Eq. (4) replaced by

$$\frac{p + \gamma p_\infty}{\gamma - 1} = \rho e = \sum_{i=1}^m \rho^{(i)} e^{(i)} = \sum_{i=1}^m \left(\frac{p^{(i)} + \gamma^{(i)} p_\infty^{(i)}}{\gamma^{(i)} - 1} \right).$$

In this instance, it is a standard approach that sets γ according to (6a) (cf. [26, 39]). Analogously, by following the same procedures as for the volume-fraction case, we find the results of p and p_∞ ,

$$p = \left(\sum_{i=1}^m \frac{p^{(i)}}{\gamma^{(i)} - 1} \right) / \left(\sum_{i=1}^m \frac{Y^{(i)}}{\gamma^{(i)} - 1} \right),$$

$$p_\infty = \left(\sum_{i=1}^m \frac{\gamma^{(i)} p_\infty^{(i)}}{\gamma^{(i)} - 1} \right) / \left(1 + \sum_{i=1}^m \frac{Y^{(i)}}{\gamma^{(i)} - 1} \right).$$

2.2. γ -based model. It is clear that the motion of the fluid mixtures, obtained from above, is governed by the Euler Eqs. (1). In the development of our multicomponent model, it is of great importance to first consider the case of an *interface only* problem where both of the pressure p and velocity u are constants in the domain, while the other variables such as ρ , γ , and P_∞ are having jumps across some interfaces.

To do so, we start out to write (1) in the following non-conservative form,

$$\begin{aligned}\frac{\partial \rho}{\partial t} + u \frac{\partial \rho}{\partial x} + \rho \frac{\partial u}{\partial x} &= 0, \\ \frac{\partial u}{\partial t} + u \frac{\partial u}{\partial x} + \frac{1}{\rho} \frac{\partial p}{\partial x} &= 0, \\ \frac{\partial}{\partial t}(\rho e) + \frac{\partial}{\partial x}(\rho e u) + p \frac{\partial u}{\partial x} &= 0,\end{aligned}$$

and obtain easily equations describing the motion of the interfaces as

$$\frac{\partial \rho}{\partial t} + u \frac{\partial \rho}{\partial x} = 0, \quad (7a)$$

$$\frac{\partial}{\partial t}(\rho e) + u \frac{\partial}{\partial x}(\rho e) = 0. \quad (7b)$$

With this, it is clear that for an interface the density ρ as well as the total internal energy ρe is evolved by the linear transport Eqs. (7a) and (7b).

To see how the pressure p would retain in equilibrium as it should be for this problem, we insert the equation of state (2) into (7b), and have

$$\frac{\partial}{\partial t} \left(\frac{p + \gamma p_\infty}{\gamma - 1} \right) + u \frac{\partial}{\partial x} \left(\frac{p + \gamma p_\infty}{\gamma - 1} \right) = 0. \quad (8)$$

By expanding (8), we may therefore write that equation as

$$\begin{aligned}\left(\frac{1}{\gamma - 1} \right) \left[\frac{\partial p}{\partial t} + u \frac{\partial p}{\partial x} \right] + p \left[\frac{\partial}{\partial t} \left(\frac{1}{\gamma - 1} \right) + u \frac{\partial}{\partial x} \left(\frac{1}{\gamma - 1} \right) \right] + \left[\frac{\partial}{\partial t} \left(\frac{\gamma p_\infty}{\gamma - 1} \right) \right. \\ \left. + u \frac{\partial}{\partial x} \left(\frac{\gamma p_\infty}{\gamma - 1} \right) \right] = 0.\end{aligned}$$

Now the requirement that p be in equilibrium leads to the equation of the form

$$p \left[\frac{\partial}{\partial t} \left(\frac{1}{\gamma - 1} \right) + u \frac{\partial}{\partial x} \left(\frac{1}{\gamma - 1} \right) \right] + \left[\frac{\partial}{\partial t} \left(\frac{\gamma p_\infty}{\gamma - 1} \right) + u \frac{\partial}{\partial x} \left(\frac{\gamma p_\infty}{\gamma - 1} \right) \right] = 0.$$

Since this equation should hold for any p in the physical space, it implies that the terms in bracket of the above equation should be vanished simultaneously, yielding a system of two equations

$$\begin{cases} \frac{\partial}{\partial t} \left(\frac{1}{\gamma - 1} \right) + u \frac{\partial}{\partial x} \left(\frac{1}{\gamma - 1} \right) = 0 \\ \frac{\partial}{\partial t} \left(\frac{\gamma p_\infty}{\gamma - 1} \right) + u \frac{\partial}{\partial x} \left(\frac{\gamma p_\infty}{\gamma - 1} \right) = 0. \end{cases} \quad (9)$$

Note that these are the evolution equations that should be satisfied for the material-dependent variables γ and p_∞ in order to have the correct pressure behavior in (8) for the interface. For convenience, we call (9) the effective equations of the problem, where the initial condition of the equations are provided, for example, by (6a) and (6c) in a respective manner.

Of course, intuitively, there are many other ways that the effective equations can be rewritten, while still getting the correct pressure from (8) for this *interface only* problem. One simple example among them is to write (9) as

$$\begin{cases} \frac{\partial}{\partial t} \left(\frac{1}{\gamma - 1} \right) + \frac{\partial}{\partial x} \left(\frac{1}{\gamma - 1} u \right) = 0 \\ \frac{\partial}{\partial t} \left(\frac{\gamma p_\infty}{\gamma - 1} \right) + \frac{\partial}{\partial x} \left(\frac{\gamma p_\infty}{\gamma - 1} u \right) = 0; \end{cases} \tag{10}$$

this is a legitimate one to use, for the velocity u is a constant for the problem (see Eqs. (25a)–(25c) also for other examples when $p_\infty = 0$). But since in general we are interested in shock wave problems as well, with the stiffened gas equation of state (2), we should only take the effective equations in a form that do not vary their solutions across both of shocks and rarefaction waves. For this reason, it rules out immediately the use of (10) as the effective equations. When further taking the numerical aspect of the model equations into consideration, it turns out that with the full Euler Eqs. (1) the effective equations in a form of (9) are the proper ones to use for practical multicomponent problems; see Section 3 for the analysis of a numerical method that approximates the model equations, and Section 4 for numerical examples.

In summary, the model equations we propose to solve multicomponent problems with the stiffened gas equation of state are

$$\begin{cases} \frac{\partial \rho}{\partial t} + \frac{\partial}{\partial x}(\rho u) = 0 \\ \frac{\partial}{\partial t}(\rho u) + \frac{\partial}{\partial x}(\rho u^2 + p) = 0 \\ \frac{\partial}{\partial t}(\rho E) + \frac{\partial}{\partial x}[(\rho E + p)u] = 0 \\ \frac{\partial}{\partial t} \left(\frac{1}{\gamma - 1} \right) + u \frac{\partial}{\partial x} \left(\frac{1}{\gamma - 1} \right) = 0 \\ \frac{\partial}{\partial t} \left(\frac{\gamma p_\infty}{\gamma - 1} \right) + u \frac{\partial}{\partial x} \left(\frac{\gamma p_\infty}{\gamma - 1} \right) = 0. \end{cases} \tag{11}$$

Here in this system the first three equations are simply the Euler Eqs. (1) that are used to make certain the conservation of ρ , ρu , and ρE , while the last two equations are the effective Eqs. (9) of the problem, that are introduced to ensure the correct mixing behavior of the variables γ and p_∞ on the interfaces.

Note the model Eqs. (11) is not written in the full conservation form, but is rather a quasi-conservative system of equations. For shock wave problems, this poses no problem at all, because for stiffened gases γ and p_∞ remain unchanged across genuinely nonlinear waves such as shocks or rarefactions, and hence we have the usual Riemann invariants and Rankine–Hugoniot jump conditions across the rarefaction and shock waves, respectively (cf. [26, 68]). At linearly degenerate waves such as interfaces where there may be jumps in γ and p_∞ , this again gives no problem since as we have seen in the previous discussion we would have the desired pressure equilibrium when the model is in use.

Of particular importance is the case of shock wave and interface interaction. It is known that, due to the nonlinearity of the problem, the pressure across the interface will be quite

different before and right after the wave interaction [7, 18]. Somewhat surprisingly, we find no major problem in using the model as well, see Section 4 for a representative numerical test. We emphasize that in this case γ and p_∞ are transported in a passive manner according to (9) along with the interface, and the variables such as ρ , u , and p are dealt with in a conservative way from the conservation part of Eqs. (11) as usual.

With all these in mind, it should be sensible to use the proposed model as for practical computations. The numerical method to be described in Section 3 is a consistent approximation of the model that gives excellent results for a wide variety of problems as illustrated in Section 4. For convenience, we call this model a γ -based model to be distinct from the other one presented below. Note in [1] Abgrall used a slightly different starting point, but nevertheless he obtained the same set of model equations for polytropic gas problems when $p_\infty = 0$.

2.3. Volume-fraction model. It should be noted that we may reformulate the above γ -based model as a volume-fraction or a mass-fraction model that is also applicable to many multicomponent problems. To demonstrate the basic idea, we consider the case in using volume-fraction functions as an example.

Similar to the approach used in the construction of our γ -based model, we look for effective equations that may preserve the pressure equilibrium for an *interface only* problem. Here with the volume-fraction notion of the states $1/(\gamma - 1)$ and $\gamma p_\infty/(\gamma - 1)$ being defined by (6a) and (6c), the key step is to replace (9) by

$$\begin{aligned} \frac{\partial}{\partial t} \left(\sum_{i=1}^m \frac{Y^{(i)}}{\gamma^{(i)} - 1} \right) + u \frac{\partial}{\partial x} \left(\sum_{i=1}^m \frac{Y^{(i)}}{\gamma^{(i)} - 1} \right) &= 0, \\ \frac{\partial}{\partial t} \left(\sum_{i=1}^m \frac{Y^{(i)} \gamma^{(i)} p_\infty^{(i)}}{\gamma^{(i)} - 1} \right) + u \frac{\partial}{\partial x} \left(\sum_{i=1}^m \frac{Y^{(i)} \gamma^{(i)} p_\infty^{(i)}}{\gamma^{(i)} - 1} \right) &= 0. \end{aligned}$$

After regrouping terms, we find the transport equation for each volume fraction $Y^{(i)}$,

$$\frac{\partial Y^{(i)}}{\partial t} + u \frac{\partial Y^{(i)}}{\partial x} = 0 \quad \text{for } i = 1, 2, \dots, m. \tag{12}$$

As before when the set of $Y^{(i)}$ is known, we may therefore compute γ and p_∞ from (6a) and (6c). In effect, in a volume-fraction model, instead of using (9) we use (12) (m of them) as the effective equations of the problem. Note that in case $Y^{(i)}$ stands for the mass-fraction of the component i , we find the effective equations of a mass-fraction model that is of the same form as in (12). Because of the close connection between the two models, we devote our discussion to one of the models only, namely to the volume-fraction model.

For completeness, we write down the full set of equations for this volume-fraction model,

$$\left\{ \begin{aligned} \frac{\partial \rho}{\partial t} + \frac{\partial}{\partial x}(\rho u) &= 0 \\ \frac{\partial}{\partial t}(\rho u) + \frac{\partial}{\partial x}(\rho u^2 + p) &= 0 \\ \frac{\partial}{\partial t}(\rho E) + \frac{\partial}{\partial x}[(\rho E + p)u] &= 0 \\ \frac{\partial Y^{(i)}}{\partial t} + u \frac{\partial Y^{(i)}}{\partial x} &= 0 \quad \text{for } i = 1, 2, \dots, m; \end{aligned} \right. \tag{13}$$

this gives us totally $m + 3$ equations to be solved. Since the derivation of the volume-fraction model comes closely out of the γ -based model, it can be shown that this model is as effective as the γ -based model. But for general multicomponent problems, the γ -based model is the preferred one to use, because the basic equations for the model stay as five, see (11), irrespective of the number of components involved in the problem.

3. NUMERICAL APPROXIMATION OF MODEL EQUATIONS

We use the high-resolution wave propagation method to compute solutions for our multicomponent models introduced in Section 2. The method is a variant of the *fluctuation-and-signal* formulation of Roe [59, 60] in that we solve the Riemann problem at each cell interface, and use the resulting waves (i.e., discontinuities propagating at constant speeds) to update the solutions in neighboring grid cells (cf. [40, 41]).

For simplicity, we describe the method on a uniform grid with fixed mesh spacing Δx , but the method can be extended quite easily to a nonuniform and time-varying grid as well [44]. We use a standard finite-volume formulation that the value $U_j^n \in \mathbb{R}^m$ approximates the cell average of the solution over the grid cell $[x_j, x_{j+1}]$ at time t_n . The time step is denoted by Δt .

In this setup, a first order accurate version of the method in wave-propagation form is a Godunov-type scheme that can be written as

$$U_j^{n+1} = U_j^n - \frac{\Delta t}{\Delta x} \sum_{k=1}^m [(\lambda_k^- \mathcal{W}_k)_j^n + (\lambda_k^+ \mathcal{W}_k)_j^n], \quad (14)$$

where $\lambda_k \in \mathbb{R}$ and $\mathcal{W}_k \in \mathbb{R}^m$ are solutions obtained from solving Riemann problems at cell interfaces x_j and x_{j+1} , $\lambda^- = \min(\lambda, 0)$, and $\lambda^+ = \max(\lambda, 0)$ (cf. [26]). It is easy to see that the method belongs to a class of upwind schemes, and as it will be shown below that the method is quasi-conservative in the sense that when applying the method to our multicomponent models not only the conservation equations but also the transport equations are approximated in a consistent manner by the method with the chosen Riemann solver. Concerning stability, it is observed numerically that the method is stable and convergent under mesh refinement provided that the waves in the method affect only the cells adjacent to the interface during the time step; see Section 4 for numerical examples and also the results shown in [43].

3.1. Method with γ -based model. Consider the γ -based model as an example. We solve the Riemann problem at each cell interface x_j that consists of (11) with piecewise constant data U_{j-1}^n and U_j^n on the left and on the right of the interface. Rather than computing the exact solution to this Riemann problem, which can be done by iterative procedures (cf. [12, 15, 54]) but is rather expensive, we use a generalized version of the approximate Riemann solver of Roe (cf. [58] and below) in most instances. This is much more efficient to compute than the exact Riemann solution, and provides a very accurate approximation of solution for smooth flows and also for moderate-strength shock waves. As long as the equation of state is not too stiff across the interfaces (which is the application considered here), the solution of the Roe Riemann solver gives a proper resolution of the contact discontinuity to be used in the method (14) for numerical approximation also. It is important to mention that in case we have a stringent set of data that involves strong shock waves and (or) stiff equation of states, we find it is advisable to use the exact Riemann solver so as to properly deal with

the nonlinear effect of the solution structure; see [67] for an example and also [20, 45, 56] for other examples that the exact Riemann solver should be in use.

To implement Roe's approximate Riemann solver, we first write (11) as a quasi-linear system of equations

$$\frac{\partial q}{\partial t} + A(q) \frac{\partial q}{\partial x} = 0 \quad (15)$$

with

$$q = \begin{pmatrix} \rho \\ \rho u \\ \rho E \\ \frac{1}{\gamma-1} \\ \frac{\gamma p_\infty}{\gamma-1} \end{pmatrix}, \quad A(q) = \begin{pmatrix} 0 & 1 & 0 & 0 & 0 \\ \left(\frac{\gamma-3}{2}\right)u^2 & (3-\gamma)u & \gamma-1 & \chi & 1-\gamma \\ \left(\frac{\gamma-1}{2}\right)u^3 - uH & H - (\gamma-1)u^2 & \gamma u & \chi u & (1-\gamma)u \\ 0 & 0 & 0 & u & 0 \\ 0 & 0 & 0 & 0 & u \end{pmatrix},$$

where $H = E + (p/\rho)$ is the enthalpy, and $\chi = -\iota(\gamma-1)^2$ with $\iota = p/(\gamma-1)$. We then solve a linear problem

$$\frac{\partial q}{\partial t} + \hat{A}(q_L, q_R) \frac{\partial q}{\partial x} = 0 \quad (16)$$

with initial data

$$q(x, 0) = \begin{cases} q_L & \text{for } x \text{ left to the interface} \\ q_R & \text{for } x \text{ right to the interface,} \end{cases}$$

where $\hat{A}(q_L, q_R)$ is a constant matrix that depends on the initial data and is a local linearization of the matrix A about an average state. Here as it is often done in many other Roe solvers (cf. [10, 23, 26]), we want to seek an average state that the difference of the fluxes in the conservation part of Eqs. (11) are equal to the respective first order approximation of the flux differences. That is,

$$\Delta \mathcal{F}^{(i)} = (\mathcal{F}_R - \mathcal{F}_L)^{(i)} = [\hat{A}(q_L, q_R)(q_R - q_L)]^{(i)} = [\hat{A}(q_L, q_R)\Delta q]^{(i)}, \quad (17)$$

for $i = 1, 2, 3$, where $\mathcal{F} \in \mathbb{R}^3$ is the usual definition of the fluxes for the Euler Eqs. (1), and $\Delta \mathcal{F}^{(i)}$ is the i th component of $\Delta \mathcal{F}$.

To accomplish the relation in (17), by taking a similar approach employed in [26] for real gases (cf. [23] also), we find it is sufficient to get the average states for variables such as \hat{u} , \hat{H} , $\hat{\gamma}$, $\hat{\iota}$, and set the matrix $\hat{A}(q_L, q_R) = A(\hat{u}, \hat{H}, \hat{\gamma}, \hat{\iota})$. The results are

$$\begin{aligned} \hat{u} &= \frac{\sqrt{\rho_L}u_L + \sqrt{\rho_R}u_R}{\sqrt{\rho_L} + \sqrt{\rho_R}}, & \hat{H} &= \frac{\sqrt{\rho_L}H_L + \sqrt{\rho_R}H_R}{\sqrt{\rho_L} + \sqrt{\rho_R}}, \\ \frac{1}{\hat{\gamma}-1} &= \frac{\sqrt{\rho_L}\left(\frac{1}{\gamma_L-1}\right) + \sqrt{\rho_R}\left(\frac{1}{\gamma_R-1}\right)}{\sqrt{\rho_L} + \sqrt{\rho_R}}, & \hat{\iota} &= \frac{\sqrt{\rho_L}\iota_L + \sqrt{\rho_R}\iota_R}{\sqrt{\rho_L} + \sqrt{\rho_R}}. \end{aligned} \quad (18)$$

Note that in the current derivation of the average states $\hat{\gamma}$ and $\hat{\iota}$ are chosen so that the expression

$$\Delta p = (\hat{\gamma}-1)^2 \left[\frac{1}{\hat{\gamma}-1} \Delta \iota - \hat{\iota} \Delta \left(\frac{1}{\gamma-1} \right) \right]$$

is satisfied approximately, and \hat{p} is computed by $(\hat{\gamma} - 1)\hat{t}$ (see [23, 24] for a related discussion to the case of real gases). As shown in Section 4, we find good results with the use of this set of average states defined in (18).

The solution of the linear problem (16) consists of five discontinuities propagating at constant speeds. The jump across each discontinuity is a multiple of the eigenvector of the matrix \hat{A} , and the propagating speed is the corresponding eigenvalue. We thus have

$$\Delta q = q_R - q_L = \sum_{k=1}^5 \hat{\alpha}_k \hat{r}_k, \quad (19)$$

where \hat{r}_k is the k th eigenvector of \hat{A} with

$$\hat{r}_1 = \begin{pmatrix} 1 \\ \hat{u} - \hat{c} \\ \hat{H} - \hat{u}\hat{c} \\ 0 \\ 0 \end{pmatrix}, \quad \hat{r}_2 = \begin{pmatrix} 1 \\ \hat{u} \\ \frac{1}{2}\hat{u}^2 \\ 0 \\ 0 \end{pmatrix}, \quad \hat{r}_3 = \begin{pmatrix} 1 \\ \hat{u} + \hat{c} \\ \hat{H} + \hat{u}\hat{c} \\ 0 \\ 0 \end{pmatrix}, \quad \hat{r}_4 = \begin{pmatrix} 0 \\ 0 \\ \hat{p} \\ 1 \\ 0 \end{pmatrix}, \quad \hat{r}_5 = \begin{pmatrix} 0 \\ 0 \\ 1 \\ 0 \\ 1 \end{pmatrix}, \quad (20)$$

and $\hat{A}\hat{r}_k = \hat{\lambda}_k \hat{r}_k$ with $\hat{\lambda}_k$ the corresponding eigenvalue,

$$\hat{\lambda}_1 = \hat{u} - \hat{c}, \quad \hat{\lambda}_2 = \hat{u}, \quad \hat{\lambda}_3 = \hat{u} + \hat{c}, \quad \hat{\lambda}_4 = \hat{\lambda}_5 = \hat{u}, \quad (21)$$

where $\hat{c} = \sqrt{(\hat{\gamma} - 1)(\hat{H} - \hat{u}^2/2)}$ is the speed of sound. The scalar $\hat{\alpha}_k$ gives the strength across the discontinuity that can be determined easily from (19). We find

$$\begin{cases} \hat{\alpha}_2 = \frac{\hat{\gamma} - 1}{\hat{c}^2} [(\hat{H} - \hat{u}^2)\Delta q^{(1)} + \hat{u}\Delta q^{(2)} - \Delta q^{(3)} + \hat{p}\Delta q^{(4)} + \Delta q^{(5)}] = \Delta p - \frac{\Delta p}{\hat{c}^2} \\ \hat{\alpha}_3 = \frac{1}{2\hat{c}} [(\hat{c} - \hat{u})\Delta q^{(1)} + \Delta q^{(2)} - \hat{c}\hat{\alpha}_2] = \frac{\Delta p + \hat{p}\hat{c}\Delta u}{2\hat{c}^2} \\ \hat{\alpha}_1 = \Delta q^{(1)} - \hat{\alpha}_2 - \hat{\alpha}_3 = \frac{\Delta p - \hat{p}\hat{c}\Delta u}{2\hat{c}^2} \\ \hat{\alpha}_4 = \Delta q^{(4)} = \Delta \left(\frac{1}{\hat{\gamma} - 1} \right) \\ \hat{\alpha}_5 = \Delta q^{(5)} = \Delta \left(\frac{\hat{\gamma} P_\infty}{\hat{\gamma} - 1} \right), \end{cases} \quad (22)$$

where $\hat{p} = \sqrt{\rho_L \rho_R}$.

Notice that in this Riemann solution there exist three discontinuities propagating at the same speed, $\hat{\lambda}_2 = \hat{\lambda}_4 = \hat{\lambda}_5 = \hat{u}$. For practical purposes, we may view these discontinuities as a single one with the operator $\hat{\mathcal{W}}_2$ defined by combining all the jumps across the $\hat{\lambda}_2$ wave family, i.e., set $\hat{\mathcal{W}}_2 = \hat{\alpha}_2 \hat{r}_2 + \hat{\alpha}_4 \hat{r}_4 + \hat{\alpha}_5 \hat{r}_5$. Clearly, doing so removes the effect of the $\hat{\lambda}_4$ and $\hat{\lambda}_5$ wave families to the solution. With this notation, we also write $\hat{\mathcal{W}}_k = \hat{\alpha}_k \hat{r}_k$ to represent the jump across the $k = 1$ and 3 waves. Wave propagation methods are based on using these propagating discontinuities to update the cells averages in the cells neighboring each interface.

We now show that in the case of an *interface only* problem the numerical solution obtained using the method would be free of oscillations, and in particular the pressure would remain

in equilibrium. Without loss of generality, we consider a single Riemann problem that at cell interface x_j the initial data are picked up so that there are no jumps in both the pressure and velocity, i.e., $\Delta p_j^n = 0$ and $\Delta u_j^n = 0$, but is otherwise for the other variables such as ρ , γ , and p_∞ . With this initial data, the Riemann solution consists of only a single contact discontinuity with the wave strength $\hat{\alpha}_{kj}$ computed by (22) as

$$\hat{\alpha}_{1j} = \hat{\alpha}_{3j} = 0, \quad \hat{\alpha}_{2j} = \Delta \rho_j^n, \quad \hat{\alpha}_{4j} = \Delta \left(\frac{1}{\gamma - 1} \right)_j^n, \quad \hat{\alpha}_{5j} = \Delta \left(\frac{\gamma p_\infty}{\gamma - 1} \right)_j^n,$$

and the associated eigen-structure \hat{r}_{kj} , $\hat{\lambda}_{kj}$ computed by (20) and (21), respectively.

Now suppose that the wave moves to the right of the interface $\hat{u}_j > 0$. To take account of the effect of this wave, according to (14), the cell average U_j^{n+1} should be evaluated by

$$\rho_j^{n+1} = \rho_j^n - \frac{\Delta t}{\Delta x} \hat{u}_j \Delta \rho_j^n, \quad (23a)$$

$$(\rho u)_j^{n+1} = (\rho u)_j^n - \frac{\Delta t}{\Delta x} \hat{u}_j [\hat{u} \Delta \rho^n]_j, \quad (23b)$$

$$(\rho E)_j^{n+1} = (\rho E)_j^n - \frac{\Delta t}{\Delta x} \hat{u}_j \left[\frac{1}{2} \hat{u}^2 \Delta \rho^n + \hat{p} \Delta \left(\frac{1}{\gamma - 1} \right)_j^n + \Delta \left(\frac{\gamma p_\infty}{\gamma - 1} \right)_j^n \right], \quad (23c)$$

$$\left(\frac{1}{\gamma - 1} \right)_j^{n+1} = \left(\frac{1}{\gamma - 1} \right)_j^n - \frac{\Delta t}{\Delta x} \hat{u}_j \Delta \left(\frac{1}{\gamma - 1} \right)_j^n, \quad (23d)$$

$$\left(\frac{\gamma p_\infty}{\gamma - 1} \right)_j^{n+1} = \left(\frac{\gamma p_\infty}{\gamma - 1} \right)_j^n - \frac{\Delta t}{\Delta x} \hat{u}_j \Delta \left(\frac{\gamma p_\infty}{\gamma - 1} \right)_j^n. \quad (23e)$$

It follows from (23a) and (23b) that we have the expected state of $u_j^{n+1} = u_j^n$ where by (18), $\hat{u}_j = u_j^n$. With this result, Eq. (23c) can be simplified to

$$(\rho e)_j^{n+1} = (\rho e)_j^n - \frac{\Delta t}{\Delta x} \hat{u}_j \left[\hat{p} \Delta \left(\frac{1}{\gamma - 1} \right)_j^n + \Delta \left(\frac{\gamma p_\infty}{\gamma - 1} \right)_j^n \right],$$

or alternatively to

$$\left(\frac{p + \gamma p_\infty}{\gamma - 1} \right)_j^{n+1} = \left(\frac{p + \gamma p_\infty}{\gamma - 1} \right)_j^n - \frac{\Delta t}{\Delta x} \hat{u}_j \left[\hat{p} \Delta \left(\frac{1}{\gamma - 1} \right)_j^n + \Delta \left(\frac{\gamma p_\infty}{\gamma - 1} \right)_j^n \right],$$

when using the equation of state (2). Notice that in case (23e) is applied to the above equation, we have further simplification

$$\left(\frac{p}{\gamma - 1} \right)_j^{n+1} = \left(\frac{p}{\gamma - 1} \right)_j^n - \frac{\Delta t}{\Delta x} \hat{u}_j \left[\hat{p} \Delta \left(\frac{1}{\gamma - 1} \right)_j^n \right],$$

and find the pressure equilibrium of the computed solution $p_j^{n+1} = p_j^n$, when Eq. (23d) is satisfied along with the fulfillment of the condition $\hat{p}_j = p_j^n$ (see (18) and the comment thereafter).

As to the behavior of the solutions ρ_j^{n+1} , γ_j^{n+1} , and $(p_\infty)_j^{n+1}$, from (23a), (23d), (23e), it is easy to derive the modified equations for each of them individually, and show monotonicity

of the results obtained using the method (cf. [42]). See results shown in Section 4 for numerical verification of this statement also.

In practical applications, there may be some other waves which come into the j th cell and affect the cell average U_j^{n+1} as well. Suppose that we are taking Riemann data at cell interface x_{j+1} so that there is a 1-wave (shock or rarefaction) propagating to the left of the interface. In this method (14), we update the cell average U_j^{n+1} by

$$\begin{aligned} \rho_j^{n+1} &:= \rho_j^{n+1} - \frac{\Delta t}{\Delta x} (\hat{u} - \hat{c})_{j+1} \left[\frac{\Delta p^n - \hat{\rho} \hat{c} \Delta u^n}{2\hat{c}^2} \right]_{j+1}, \\ (\rho u)_j^{n+1} &:= (\rho u)_j^{n+1} - \frac{\Delta t}{\Delta x} (\hat{u} - \hat{c})_{j+1} \left[(\hat{u} - \hat{c}) \left(\frac{\Delta p^n - \hat{\rho} \hat{c} \Delta u^n}{2\hat{c}^2} \right) \right]_{j+1}, \\ (\rho E)_j^{n+1} &:= (\rho E)_j^{n+1} - \frac{\Delta t}{\Delta x} (\hat{u} - \hat{c})_{j+1} \left[(\hat{H} - \hat{u} \hat{c}) \left(\frac{\Delta p^n - \hat{\rho} \hat{c} \Delta u^n}{2\hat{c}^2} \right) \right]_{j+1}. \end{aligned}$$

We note that due to a fundamental property of the Roe solver, i.e., the relation in (17), this is a conservative update of the numerical solutions ρ_j^{n+1} , $(\rho u)_j^{n+1}$, and $(\rho E)_j^{n+1}$. We get a new pressure p_j^{n+1} by using the equation of state (2),

$$p_j^{n+1} = (\gamma_j^{n+1} - 1) \left(\rho E - \frac{1}{2} \rho u^2 \right)_j^{n+1} - (\gamma p_\infty)_j^{n+1}.$$

One advantage of using the wave propagation form is that we are able to handle each wave in turn, and there is no need to compute fluxes and make distinction between the waves (cf. [67]). Extension of the method to higher order accuracy, and in particular to a high-resolution version of the wave propagation scheme, follows easily by incorporating limited slopes and by constructing piecewise linear profiles to the method; see [43, 44] for the detail. It is not difficult to show that for the *interface* only problem we again have the required pressure equilibrium that is independent of the limiter being employed to the high-resolution method. Moreover, we obtain a better resolution of the result as compared to the first order result; see Section 4 for numerical examples.

3.2. Method with volume-fraction model. We now consider the use of the Riemann solutions associated with the volume-fraction model (13) to the wave propagation method (14). For simplicity in description, we are concerned with a two-component flow problem that the quasi-linear system of equations in (15) are defined with

$$q = \begin{pmatrix} \rho \\ \rho u \\ \rho E \\ Y^{(1)} \\ Y^{(2)} \end{pmatrix}, \quad A(q) = \begin{pmatrix} 0 & 1 & 0 & 0 & 0 \\ \left(\frac{\gamma-3}{2}\right)u^2 & (3-\gamma)u & \gamma-1 & \chi^{(1)} & \chi^{(2)} \\ \left(\frac{\gamma-1}{2}\right)u^3 - uH & H - (\gamma-1)u^2 & \gamma u & \chi^{(1)}u & \chi^{(2)}u \\ 0 & 0 & 0 & u & 0 \\ 0 & 0 & 0 & 0 & u \end{pmatrix},$$

where $\chi^{(i)} = (1 - \gamma)(p + \gamma^{(i)} p_\infty^{(i)}) / (\gamma^{(i)} - 1)$. We use the Roe solver as usual in that we solve the linear problem (16) with the Roe-type matrix $\hat{A}(q_L, q_R) = A(\hat{u}, \hat{H}, \hat{c}, \hat{Y}^{(1)}, \hat{Y}^{(2)})$ depending on the initial data q_L and q_R . Here as in the case of the γ -based model we

compute the average states \hat{u} , \hat{H} , \hat{t} by (18), and set the average state $\hat{Y}^{(i)}$ by the standard “Roe-averaging” approach also with

$$\hat{Y}^{(i)} = \frac{\sqrt{\rho_L} Y_L^{(i)} + \sqrt{\rho_R} Y_R^{(i)}}{\sqrt{\rho_L} + \sqrt{\rho_R}} \quad \text{for } i = 1, 2.$$

When defining \hat{A} in this way, it is easy to check the satisfaction of the fundamental relation in (17).

The result of this linearized Riemann problem takes a rather similar wave structure as to the form shown in (19)–(22) of the γ -based model. Without writing the full solution here, we mention that the only difference between the representation of these two solutions is to the jump across the $\hat{\lambda}_4$ and $\hat{\lambda}_5$ families. Here we use the following expressions instead,

$$\hat{\alpha}_4 = \Delta Y^{(1)}, \quad \hat{\alpha}_5 = \Delta Y^{(2)}, \quad \hat{r}_4 = \begin{pmatrix} 0 \\ 0 \\ \frac{\hat{p} + \gamma^{(1)} p_\infty^{(1)}}{\gamma^{(1)} - 1} \\ 1 \\ 0 \end{pmatrix}, \quad \hat{r}_5 = \begin{pmatrix} 0 \\ 0 \\ \frac{\hat{p} + \gamma^{(2)} p_\infty^{(2)}}{\gamma^{(2)} - 1} \\ 0 \\ 1 \end{pmatrix}.$$

As in the case performed for the γ -based model, we now analyze the pressure obtained using the method (14) with the volume-fraction model for the *interface only* problem considered there. In this case, it is enough to begin looking at the update of the internal energy in the form,

$$\left(\frac{p + \gamma p_\infty}{\gamma - 1} \right)_j^{n+1} = \left(\frac{p + \gamma p_\infty}{\gamma - 1} \right)_j^n - \frac{\Delta t}{\Delta x} \hat{u}_j \left[\sum_{i=1}^2 \frac{\hat{p} + \gamma^{(i)} p_\infty^{(i)}}{\gamma^{(i)} - 1} \Delta (Y^{(i)})^n \right]_j.$$

Note the above equation is just a simplified version of the update of the total energy by taking into account of the fact that $u_j^{n+1} = u_j^n$. When substituting the volume-fraction relations in (6a) and (6c) for γ and p_∞ , we may write the equation as

$$\begin{aligned} \left(\sum_{i=1}^2 \frac{Y^{(i)} p}{\gamma^{(i)} - 1} + \frac{Y^{(i)} \gamma^{(i)} p_\infty^{(i)}}{\gamma^{(i)} - 1} \right)_j^{n+1} &= \left(\sum_{i=1}^2 \frac{Y^{(i)} p}{\gamma^{(i)} - 1} + \frac{Y^{(i)} \gamma^{(i)} p_\infty^{(i)}}{\gamma^{(i)} - 1} \right)_j^n \\ &- \frac{\Delta t}{\Delta x} \hat{u}_j \left[\sum_{i=1}^2 \frac{\hat{p} + \gamma^{(i)} p_\infty^{(i)}}{\gamma^{(i)} - 1} \Delta (Y^{(i)})^n \right]_j. \end{aligned}$$

After a simple manipulation, we find $p_j^{n+1} = p_j^n$, only if $\hat{p}_j = p_j^n$ and the establishment of the difference equations for the volume fraction $Y^{(i)}$,

$$(Y^{(i)})_j^{n+1} = (Y^{(i)})_j^n - \frac{\Delta t}{\Delta x} \hat{u}_j \Delta (Y^{(i)})_j^n \quad \text{for } i = 1, 2.$$

It is easy to see that the latter two requirements are guaranteed by the method.

Note for this two-component flow problem we have described the method uses two different volume-fraction functions $Y^{(1)}$ and $Y^{(2)}$. In practice, due to the fact that $Y^{(1)} + Y^{(2)} = 1$, we may simply use a volume-fraction function, say $Y^{(1)}$, to the model, and set the

value of the other one, $Y^{(2)} = 1 - Y^{(1)}$, for example. When modeling in this way, it gives a more robust method to the computation of two-component flow problems than the use of the γ -based model to the method.

4. NUMERICAL RESULTS IN ONE DIMENSION

We now present results to validate our multicomponent algorithm with the Roe solver described in Section 3 in one dimension.

EXAMPLE 4.1. We consider an *interface only* problem that the solution of a Riemann problem consists of a single contact discontinuity in gas dynamics. We take two sets of data for numerical experiments. In the first set, we have a polytropic gas and use two constant states as

$$\begin{pmatrix} \rho \\ u \\ p \\ \gamma \\ p_\infty \end{pmatrix}_L = \begin{pmatrix} 1 \\ 1 \\ 1 \\ 1.4 \\ 0 \end{pmatrix} \quad \text{and} \quad \begin{pmatrix} \rho \\ u \\ p \\ \gamma \\ p_\infty \end{pmatrix}_R = \begin{pmatrix} 0.125 \\ 1 \\ 1 \\ 1.2 \\ 0 \end{pmatrix}, \quad (24)$$

while in the second set we use the same data as in the first set with the exception that on the state R a stiffened gas with $\gamma_R = 4$ and $(p_\infty)_R = 1$ is employed instead. Here L is the state used for $x \in [0, 0.2)$ and R is the state used for $x \in [0.2, 1]$.

Results for the first set of data are shown in Fig. 1 where we have employed the γ -based model together with both the first order and high-resolution wave propagation methods to the computations. For comparison, we also include results obtained using three different effective equations to the simulations. They are the conservation equations with either

$$\frac{\partial}{\partial t}(\rho\gamma) + \frac{\partial}{\partial x}(\rho\gamma u) = 0, \quad (25a)$$

or

$$\frac{\partial}{\partial t}\left(\frac{\rho}{\gamma - 1}\right) + \frac{\partial}{\partial x}\left(\frac{\rho u}{\gamma - 1}\right) = 0, \quad (25b)$$

and the primitive equation

$$\frac{\partial \gamma}{\partial t} + u \frac{\partial \gamma}{\partial x} = 0. \quad (25c)$$

Note in the cases of (25a) and (25b), we have two model systems that are in the full conservation form; see [34] for a similar consideration.

From the figure, we clearly observe pressure fluctuations in the solutions when employing any of the equations in (25a)–(25c), but not the γ -based model where (9) is considered, to the method. By following a similar analysis conducted in Section 3 for an *interface only* problem, we may explain the observed error behavior in pressure as being the failure to approximate the energy Eq. (7b) in a consistent manner when those equations are in use (cf. [34]). Note other variables in the solution are affected by this error also as time evolves. Numerical evidences suggest however that these errors decrease as the mesh is refined, and

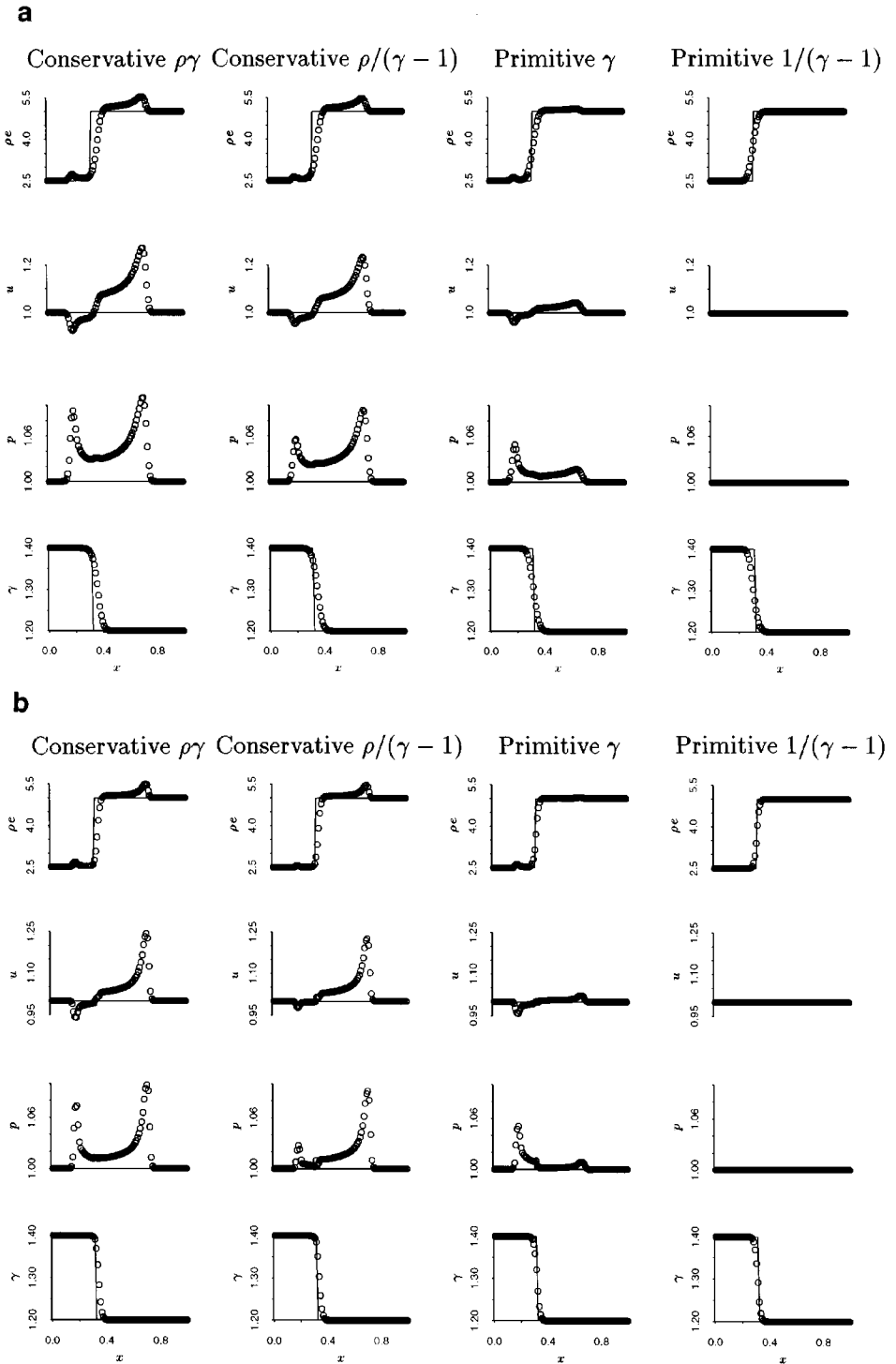


FIG. 1. Comparison plots of four different multicomponent models for the Euler equations with data (24) at time $t = 0.12$. (a) Results using the first order wave propagation method. (b) Results using the high-resolution wave propagation method with the “minmod” slope limiter. In each figure the solid line is the exact solution and the points show the computed solution with 100 mesh points.

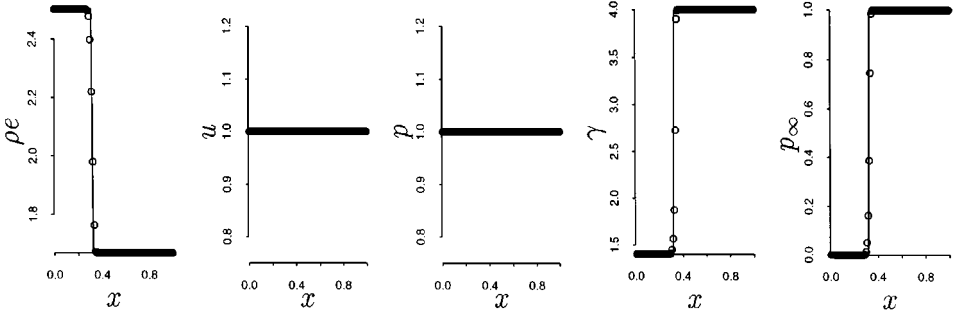


FIG. 2. High-resolution results for an *interface* only problem using the same initial data as in Fig. 1 with the exception that $\gamma_R = 4$ and $(p_\infty)_R = 1$ are used in the current computation. The solid line is the exact solution and the points show the computed solution with 100 mesh points.

the rate of convergence of the error in the 1-norm is about the order of accuracy of the method that is employed to the computation.

Figure 2 shows results of a run using the second set of data where only the high-resolution solutions with the γ -based model are presented. Notice that the pressure and also the velocity remain at constant states for this stiffened gas simulation. Because the errors become too erroneous in most cases, we do not show results using the type of models given in (25a)–(25c) for this test.

Note in the above computation, we use 100 mesh points and plot the results at time $t = 0.12$. For the purposes in illustration of the basic solution structure obtained from using the high-resolution version of the method, we only present results using the simpler “minmod” slope limiter (see [42, 70]) for the runs. Of course, other more sophisticated limiters, such as “superbee” for example (cf. [2, 70]), can be employed to the methods for computations also. As far as the global structure of the solution is concerned, we observe quite similar behavior of the solutions when different limiters are in use to the method. We further remark that the Courant number (see [42]) in choosing the time step that maintains stability of the method is 0.9 in the tests. The nonreflecting boundaries are used on the left and right of the computational domain. Without further notice, we use the same limiter and the Courant number for all other experiments performed in this paper.

EXAMPLE 4.2. We next are concerned with a two-phase gas-liquid Riemann problem. On the left when $x \in [0, 0.5)$, we have the gas phase with data

$$(\rho, u, p, \gamma, p_\infty)_L = (1.241, 0, 2.753, 1.4, 0),$$

and on the right when $x \in [0.5, 1]$, we have the liquid phase with data

$$(\rho, u, p, \gamma, p_\infty)_R = (0.991, 0, 3.059 \times 10^{-4}, 5.5, 1.505).$$

We note that the above variables have been nondimensionalized as in the work done by Cocchi *et al.* [12] and Cooke and Chen [17] to simulate underwater explosions in a spherically symmetric geometry. We run the problem in a shock tube with 100 mesh points, and show the high-resolution results in Fig. 3 at time $t = 0.1$ using the γ -based model. From the figure, we again see the correct behavior of the computed contact discontinuity, and

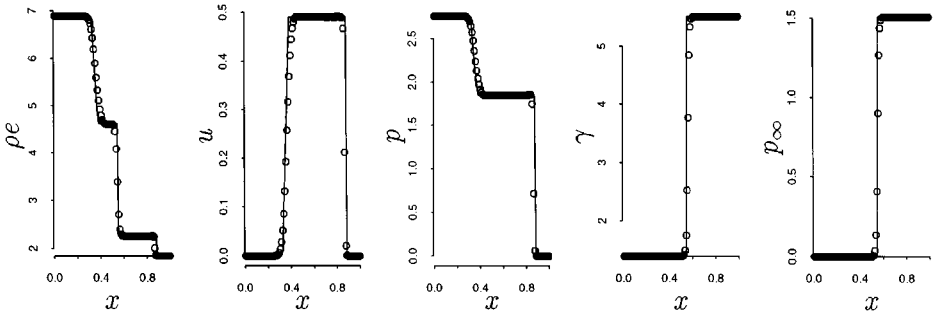


FIG. 3. High-resolution results for a two-phase gas-liquid Riemann problem at time $t = 0.1$. The solid line is the exact solution and the points show the computed solution with 100 mesh points.

also the rarefaction and shock waves as in comparison with the exact solution (the solid line shown in the plot). The results of this problem with a source term that accounts for the simplification of a cylindrically symmetric flow will be presented in Section 5 together with two-dimensional results.

EXAMPLE 4.3. Finally, we consider a shock-contact interaction problem studied by Abgrall [1] and Karni [35] that verifies convergence of the computed solutions to the correct weak ones in a multicomponent case. The initial condition we use consists of a stationary interface at $x = 0.5$ separating two fluids of different equation of states, and a leftward going Mach 1.95 shock wave at $x = 0.6$ traveling from the right to left. The gas on the left of the interface is a polytropic gas with

$$(\rho, u, p, \gamma, p_\infty)_L = (1, 0, 1, 1.4, 0),$$

and the gas on the right of the interface (i.e., on the middle and the preshock state), is a stiffened gas with

$$(\rho, u, p, \gamma, p_\infty)_M = (5, 0, 1, 4, 1).$$

The state behind the shock is

$$(\rho, u, p, \gamma, p_\infty)_R = (7.093, -0.7288, 10, 4, 1).$$

The exact solution for this problem in the $x-t$ plane up to time $t = 0.2$ is illustrated in Fig. 4 where the density contours are presented.

A snap shot of the computed total internal energy, velocity, and pressure are shown in Fig. 5 at time $t = 0.2$ where we solve the problem using the high-resolution wave propagation method with 200 mesh points. We can easily see that the shock wave and contact discontinuity are very well located, and the rarefaction wave moves at the correct speed with the correct shape. A two-dimensional version of the problem will be considered in Section 6.

We note that in this section we have only present numerical solutions obtained using the γ -based model to the method. It is interesting to mention that we find little difference between the results as compared to the ones obtained using the volume-fraction model to the method for simulations. Because of this, we omit the presentation of the volume-fraction based numerical results here.

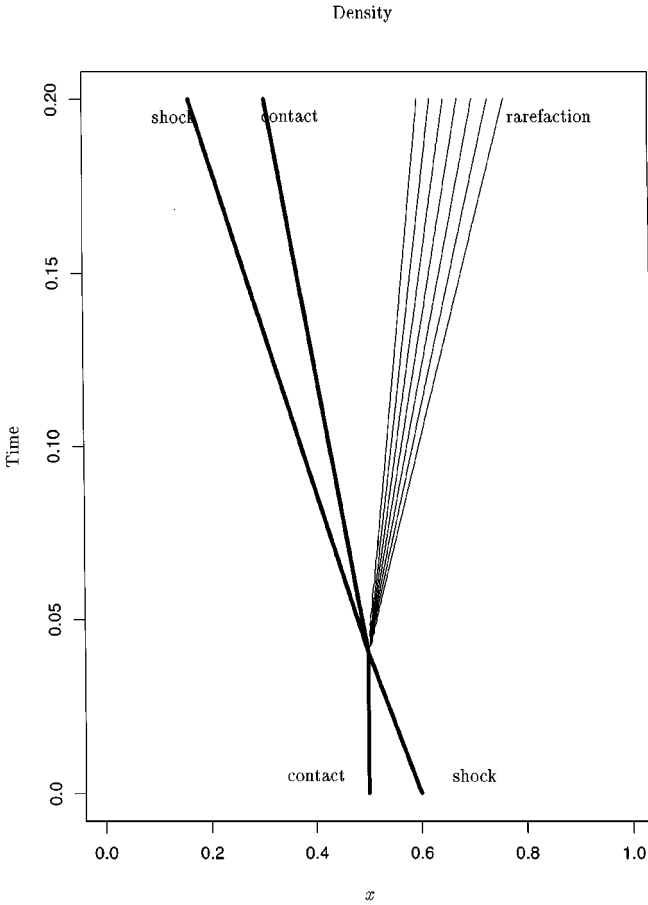


FIG. 4. The exact solution for a shock-contact interaction problem for the Euler equations with a stiffened gas equation of state; density contour plot in the x - t plane.

5. EXTENSION TO MULTIPLE DIMENSIONS

The two-dimensional version of the γ -based model for compressible multicomponent problems with the stiffened gas equation of state takes the form

$$\left\{ \begin{array}{l} \frac{\partial \rho}{\partial t} + \frac{\partial}{\partial x}(\rho u) + \frac{\partial}{\partial y}(\rho v) = 0 \\ \frac{\partial}{\partial t}(\rho u) + \frac{\partial}{\partial x}(\rho u^2 + p) + \frac{\partial}{\partial y}(\rho uv) = 0 \\ \frac{\partial}{\partial t}(\rho v) + \frac{\partial}{\partial x}(\rho uv) + \frac{\partial}{\partial y}(\rho v^2 + p) = 0 \\ \frac{\partial}{\partial t}(\rho E) + \frac{\partial}{\partial x}[(\rho E + p)u] + \frac{\partial}{\partial y}[(\rho E + p)v] = 0 \\ \frac{\partial}{\partial t} \left(\frac{1}{\gamma - 1} \right) + u \frac{\partial}{\partial x} \left(\frac{1}{\gamma - 1} \right) + v \frac{\partial}{\partial y} \left(\frac{1}{\gamma - 1} \right) = 0 \\ \frac{\partial}{\partial t} \left(\frac{\gamma p_\infty}{\gamma - 1} \right) + u \frac{\partial}{\partial x} \left(\frac{\gamma p_\infty}{\gamma - 1} \right) + v \frac{\partial}{\partial y} \left(\frac{\gamma p_\infty}{\gamma - 1} \right) = 0. \end{array} \right. \quad (26)$$

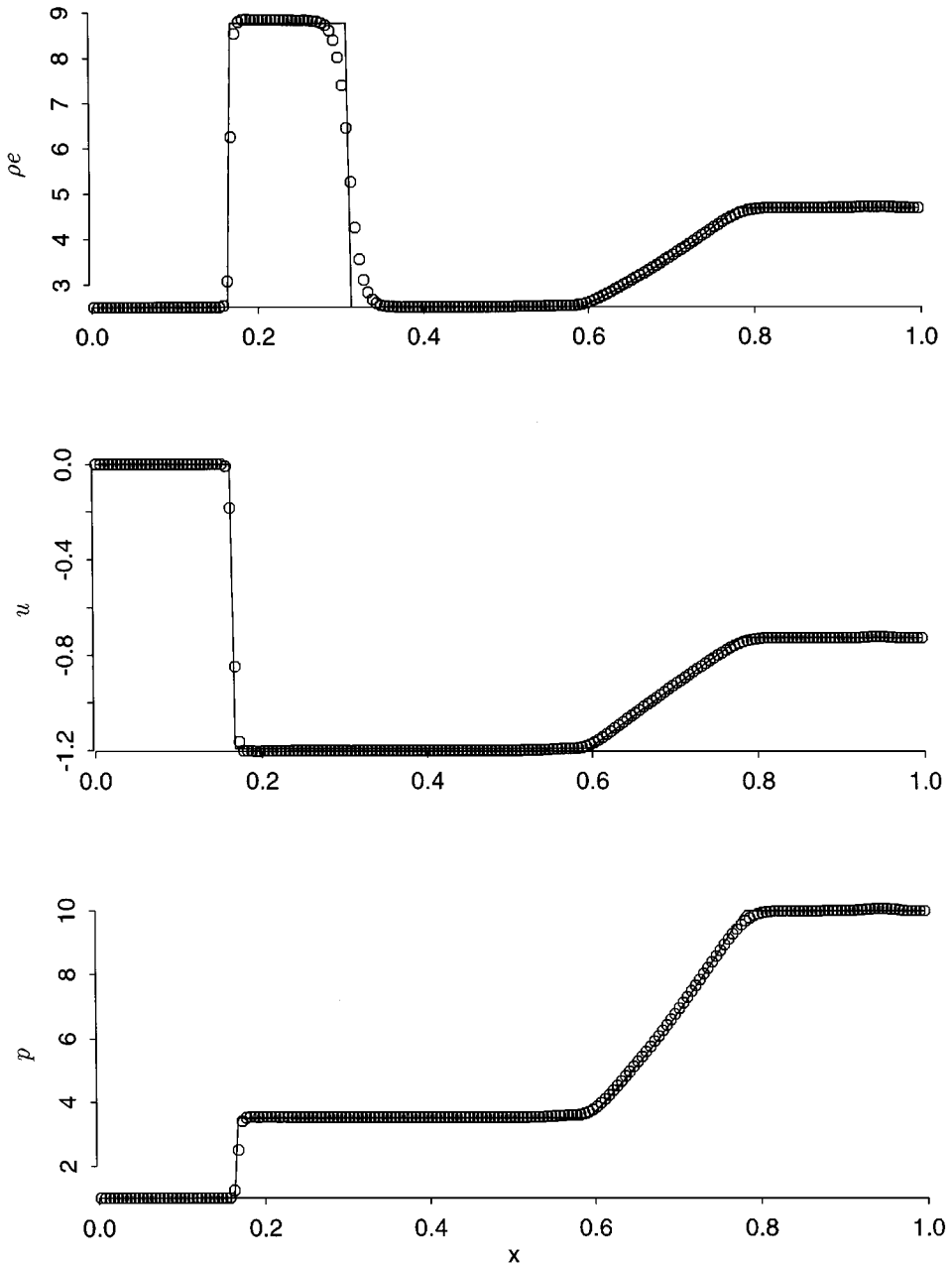


FIG. 5. Results for a shock-contact interaction problem; snap shot of the density, velocity, and pressure at time $t = 0.2$ with 200 mesh points. The solid line is the exact solution.

Here u and v are the velocities in the x - and y -direction, respectively, and $E = e + (u^2 + v^2)/2$. In this model system, the first four components are simply the Euler equations in two dimensions that describe the conservation of mass, momenta in the x - and y -direction, and energy of the problems [18]. As in the one-dimensional case (see Section 2), the last two components are the effective equations that are derived to model the motions of the thermodynamics variables γ and p_∞ near the material interfaces. We take the effective

equations to be of the form as shown in (26) that is suitable for numerical approximation of the model to practical multicomponent problems.

Here we use a two-dimensional generalization of the high-resolution wave propagation method to compute solutions of this model. In the method, waves obtained from solving one-dimensional Riemann problems in the directions normal and tangential to the cell interfaces are used to update the solutions in neighboring cells with the slopes and limiters that are introduced to achieve high resolutions (cf. [40, 41, 43, 45]). Two sample calculations are presented below to validate the method with the Roe approximate Riemann solver where the exact or “true” solution is available for the test cases; see the next section for more results.

EXAMPLE 5.1. We begin by considering an *interface only* problem that the solution consists of a circular interface with radius $r_0 = 0.16$ evolving in a constant velocity field $(u, v) = (1, 1)$. We take the same initial data as in Example 4.1 that the pressure is continuous across the interface with $p = 1$, while the density, γ , and p_∞ are set by

$$(\rho, \gamma, p_\infty) = \begin{cases} (1, 1.4, 0) & \text{for } r < r_0 \\ (0.125, 4, 1) & \text{for } r > r_0, \end{cases}$$

where $r^2 = (x - x_0)^2 + (y - y_0)^2$ is the distance from the center $(x_0, y_0) = (0.25, 0.25)$. The results of one sample test are shown in Figs. 6–9 where the 3D surface plots of the density and pressure are presented at time $t = 0.36$. The cross section of the density and pressure along the $x = y$ line are plotted in the figure also where the solid line is the exact solution. It is easy to observe good agreement of the results. Notice in particular that the

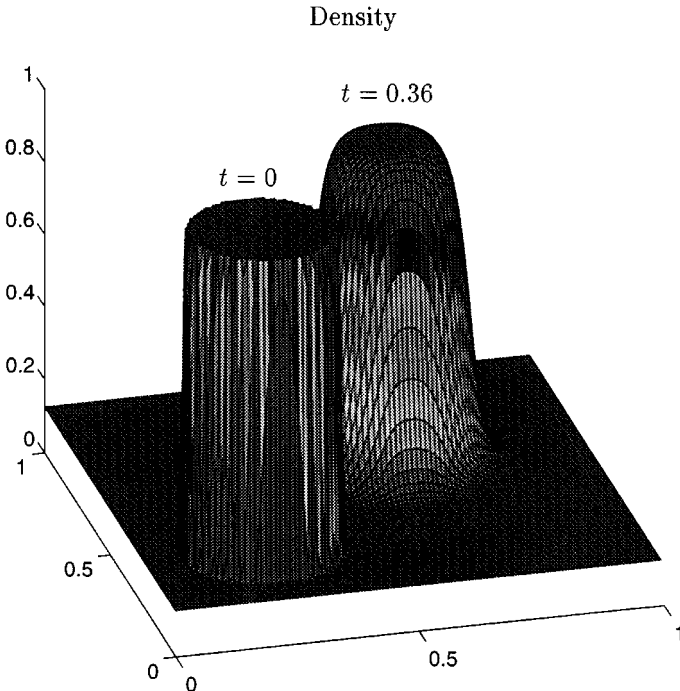


FIG. 6. High-resolution results for an interface-evolving problem at time $t = 0.36$, surface plots of the density.

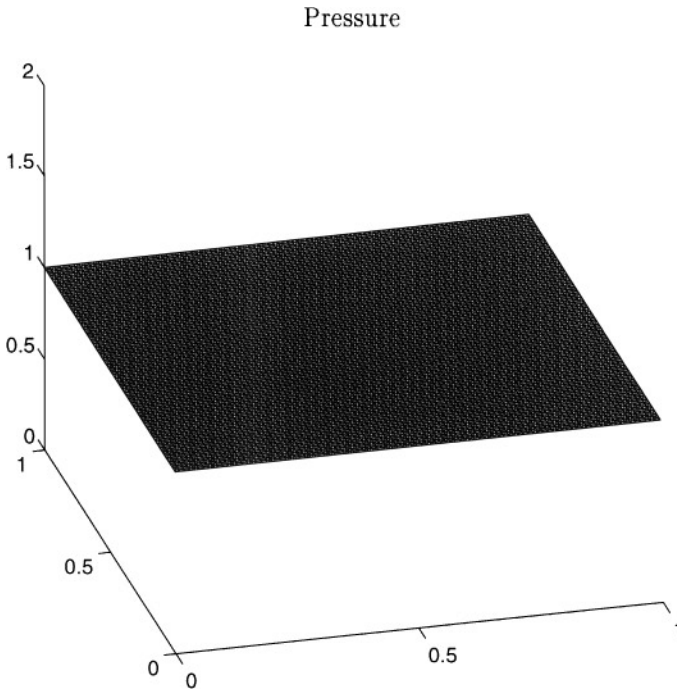


FIG. 7. High-resolution results for an interface-evolving problem at time $t = 0.36$, surface plots of the pressure.

computed pressure is staying in equilibrium as desired. In this computation we have used the high resolution version of the method with a 100×100 grid and the usual Courant number 0.9 and the “minmod” limiter.

EXAMPLE 5.2. We next consider a radially symmetric problem that due to the pressure difference an initially at rest circular air bubble is exploded under the water. We use the same set of data as in Example 4.2 that inside the bubble of radius $r_0 = 0.2$, the fluid is air with

$$(\rho, p, \gamma, p_\infty) = (1.241, 2.753, 1.4, 0),$$

while outside the bubble, the fluid is water with

$$(\rho, p, \gamma, p_\infty) = (0.991, 3.059 \times 10^{-4}, 5.5, 1.505).$$

For this problem, we perform the computation using the high-resolution method with a 100×100 grid, and obtain the results for the density and pressure as shown in Fig. 10. From the contours of the plots, it is easy to see that breaking of the bubble results in an outgoing circular shock wave and an incoming rarefaction wave; the contact discontinuity lies in between these waves. From the cross-sectional plots along line $y = 0.5$, we find good agreement of the results as compared with the “true” solution obtained from solving the one-dimensional multicomponent model with appropriate source terms for the radial symmetry using the front-tracking algorithm [44] (with 500 mesh points). Here the pressure near the interface behaves in a satisfactory manner without any spurious oscillations, and the shock wave and contact discontinuity appear to be very well located.

To end this section, we note that, as in the one-dimensional case, we may form a two-dimensional version of the volume-fraction model by simply replacing the effective equations in (26) with the set of equations for the volume-fraction function $Y^{(i)}$,

$$\frac{\partial Y^{(i)}}{\partial t} + u \frac{\partial Y^{(i)}}{\partial x} + v \frac{\partial Y^{(i)}}{\partial y} = 0 \quad \text{for } i = 1, 2, \dots, m \quad (27)$$

of an m -component problem. As soon as $Y^{(i)}$ is known, the computation of γ and p_∞ can be done in the same way as in the one-dimensional case. Again, we observe not much difference between the computed solutions when comparing the results obtained using the γ -based and volume-fraction formulations of the algorithm to various multicomponent problems.

By analogy with the two-dimensional extension, it is easy to construct the multicomponent models in three dimensions. We may then solve the resulting model equations using three-dimensional wave propagation methods of the type described in [37], for example. The results of the computations will be reported in a sequel paper in the future.

6. RICHTMYER-MESHKOV INSTABILITY

We now present numerical results to the simulation of Richtmyer–Meshkov unstable interface problems in two dimensions. Our goal of the tests performed here is twofold: the first is to validate convergence of the computed solutions obtained using our multicomponent algorithm to the correct weak ones, and the second is to provide an example that shows the effectiveness of the algorithm to practical problems.

To set up the test, we consider a shock tube with length 4 and height 1 in a two-dimensional domain. In the standard Richtmyer–Meshkov unstable interface problem, the initial condition in the tube is composed of an interface separating two fluids of different densities and a shock wave approaching the interface. It is known that this interface becomes unstable (i.e., the amplitude of the initial perturbation to the interface is growing with respect to time) after the passage of a shock wave, irrespective of the side of the heavy or light fluid that the shock is incident upon (cf. [32, 57, 61, 75]). We note that this behavior of the interface is unlike the gravity-induced Rayleigh–Taylor instability where the interface is unstable only when the heavy fluid lies above the light fluid; assuming gravity is directed *downwards* (cf. [22, 64]).

EXAMPLE 6.1. We take a single mode perturbation of an air-SF₆ interface that the initial location of the interface is represented by

$$x = x_0 + \varepsilon \cos(2\pi ky) \quad \text{for } y \in [0, 1], \quad (28)$$

where $x_0 = 1.2$ is the location of the unperturbed interface, $\varepsilon = 0.1$ is the amplitude of the perturbation, and $k = 1$ is the wave number. We use the polytropic gas equation of state for air and SF₆ with $\gamma = 1.4$ and $\gamma = 1.093$, respectively. We choose the density ratio $D = \rho_{\text{SF}_6} / \rho_{\text{air}} = 5.04$ so as to maintain the constant pressure and temperature across the interface. To trigger the instability, at $x = 1.325$ there is a planar Mach 1.24 shock wave in air propagating from the left to the right of the interface. This gives us one example that the interface is accelerated by a shock wave coming from the light-fluid to the heavy-fluid region, and the resulting wave pattern after the interaction would consist of a transmitted shock wave, an interface, and a reflected shock.

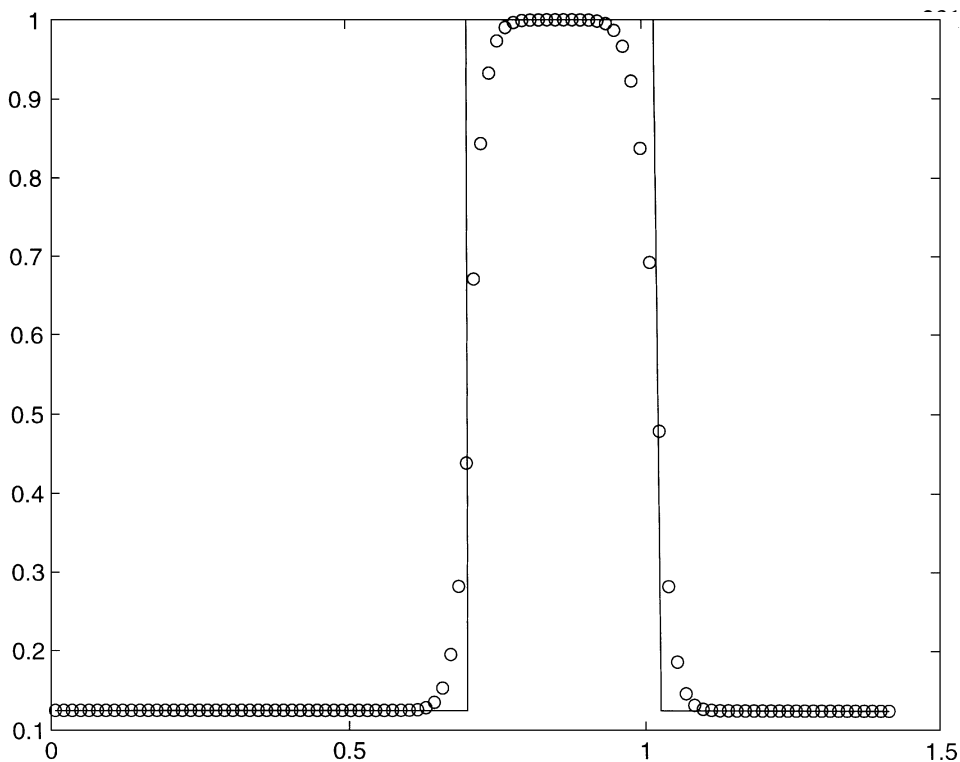


FIG. 8. High-resolution results for an interface-evolving problem at time $t = 0.36$, cross-sectional plot the density.

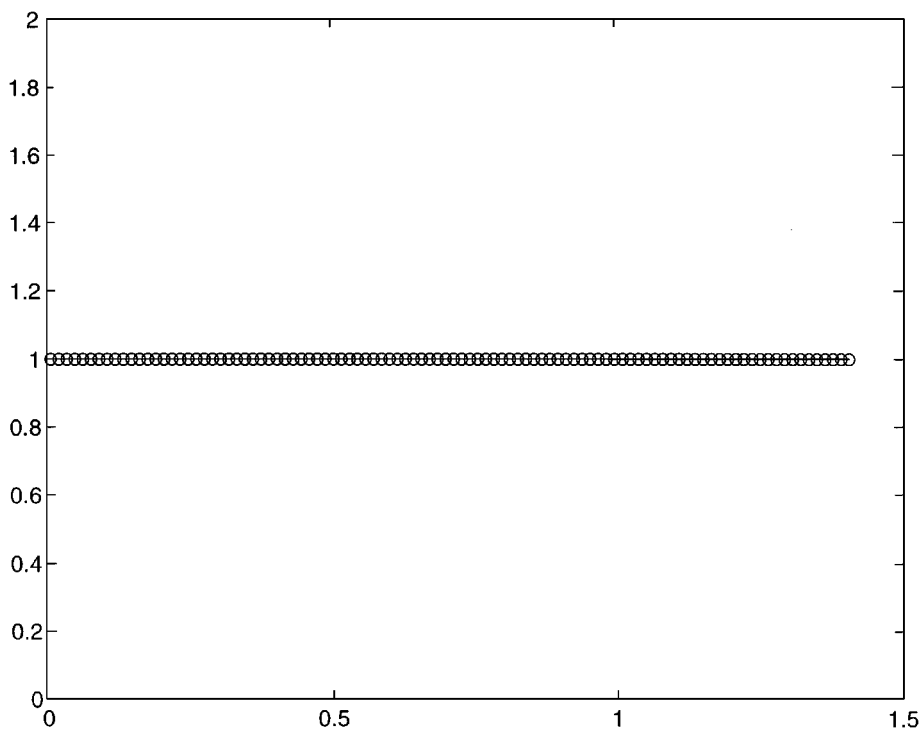


FIG. 9. High-resolution results for an interface-evolving problem at time $t = 0.36$, cross-sectional plot the pressure.

We use the high-resolution wave propagation method with the γ -based model for the computation. We consider a 320×80 grid with periodic boundaries on the top and bottom and nonreflecting boundaries on the left and right. The results are presented in Fig. 11 where the contours of the density and pressure (in logarithmic scale) are shown at six different times. Note that the dashed line in each pressure contours is the $\psi = 0$ level set introduced in the simulation as a passive quantity for representing the approximate location of the interface (see [52, 53, 63] for more information on the use of level set functions to general moving-front problems). From the figure, it is easy to see the growth of the interface and also the complicated wave patterns that are induced by this wave interaction.

To check the correctness of the computed solutions, Fig. 12 compares the cross section of the results for the same run along line $y = 0.5$ with the results obtained using the front-tracking version of the method (see [45] for the details of the front-tracking method). Good agreement of the solutions is clearly observed; see Fig. 13 also for a comparison of the interface locations. In Fig. 14, we show results for a convergence study performed using a mesh refinement sequence: $2^i (80 \times 20)$ for $i = 0, 1, 2$, where the density and pressure cross-sectional solutions along line $y = 0.5$ are plotted at time $t = 9$. Notice that the reasonable

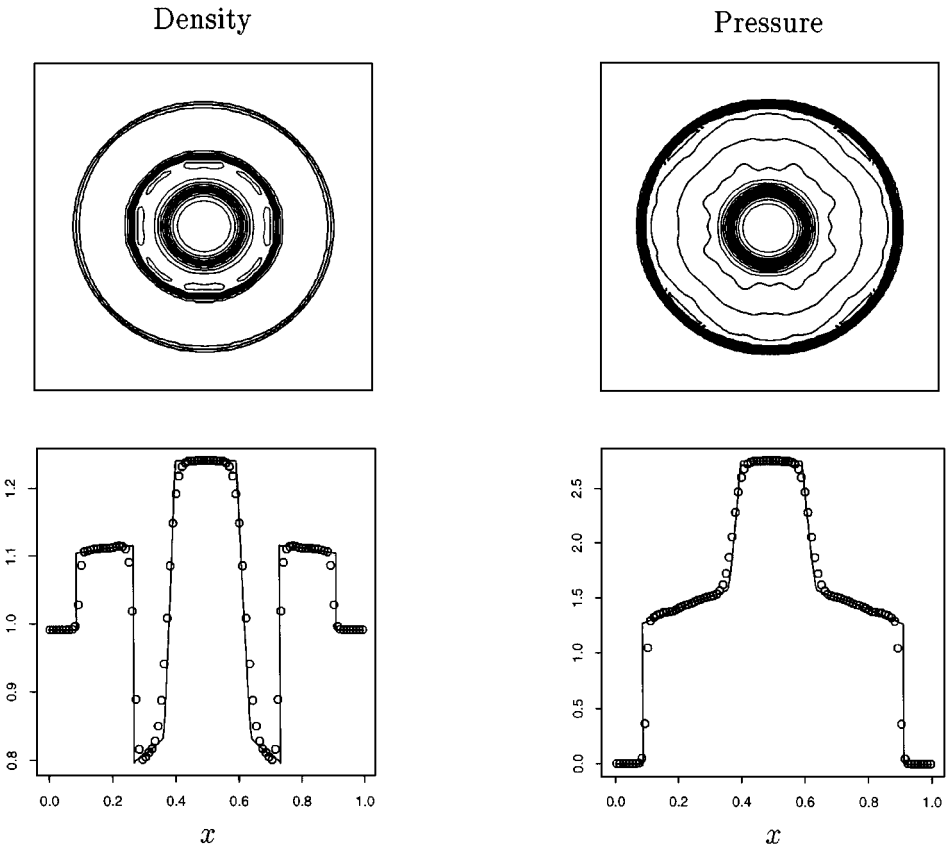


FIG. 10. Results for a radially symmetric problem at time $t = 0.058$. Contours of the density and pressure are shown together with the cross-section of the solutions along line $y = 0.5$. The solid line in the cross-section plot is the “true” solution obtained from solving the one-dimensional multicomponent model with appropriate source terms for the radial symmetry using the front-tracking algorithm. The dotted points are the two-dimensional result obtained using the high-resolution wave propagation method.

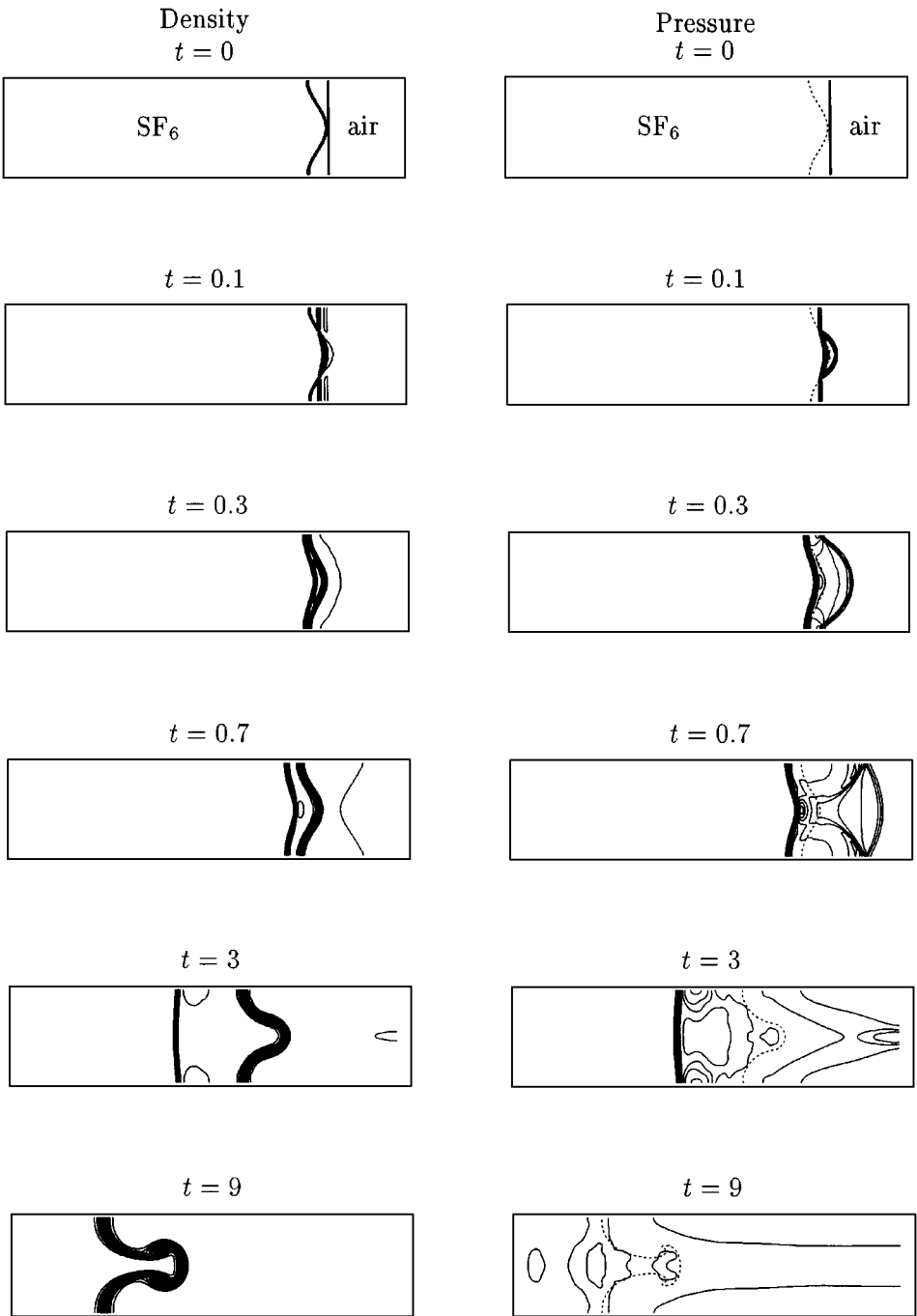


FIG. 11. Results for the simulation of Richtmyer–Meshkov instability, a Mach 1.24 shock wave in air, and an air-SF₆ interface case. The density and pressure contours (in logarithmic scale) are shown at six different times obtained using the high-resolution wave propagation method with a 320 × 80 grid. The dashed line in the pressure contour plot is the $\psi = 0$ level set introduced in the simulation as a passive quantity for representing the approximate location of the interface.

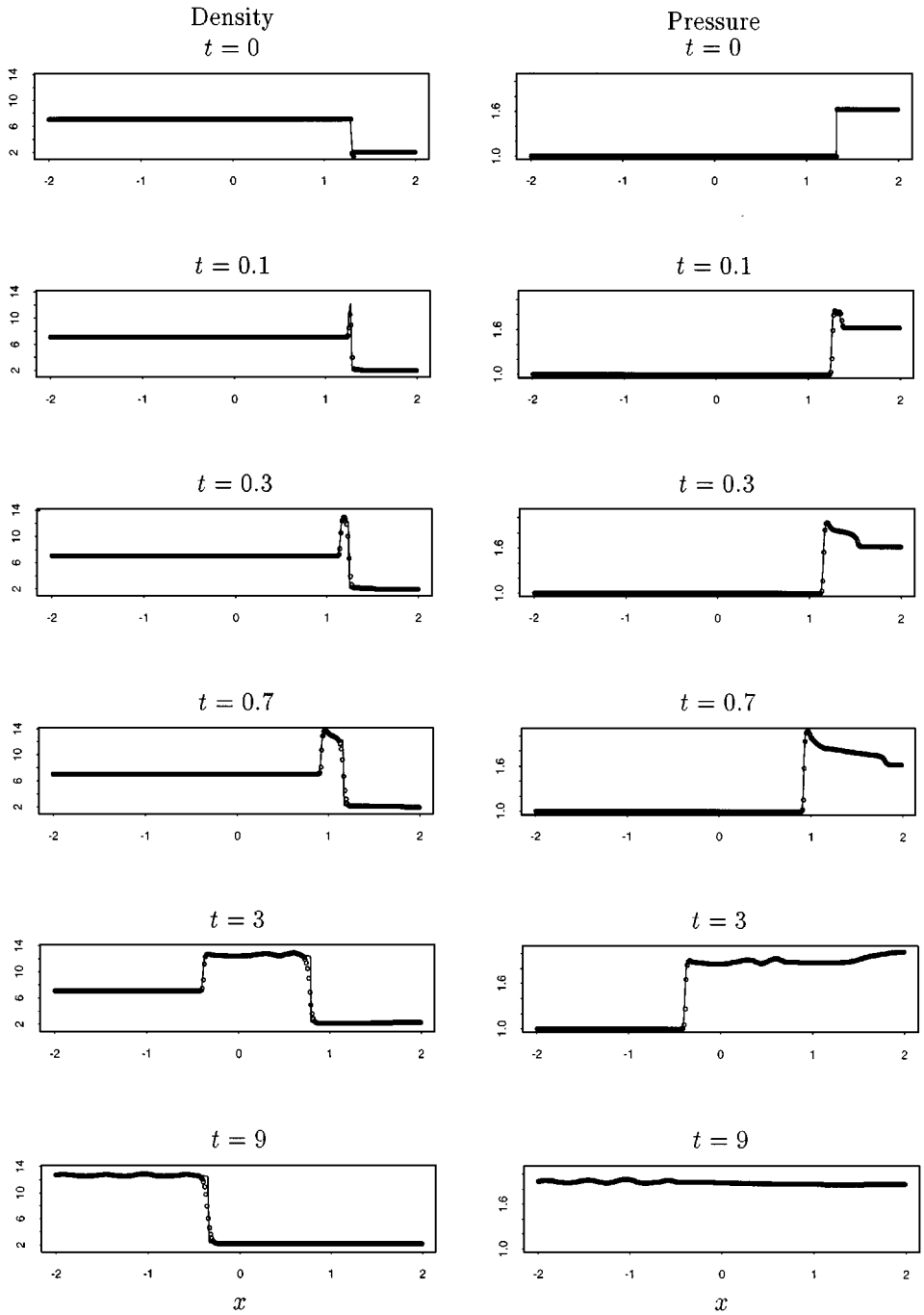
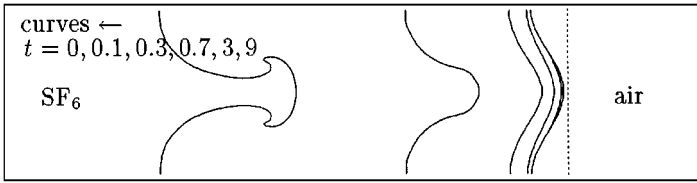


FIG. 12. The cross-sectional plots of the results for the run shown in Fig. 11 along line $y = 0.5$, where the solid lines are results obtained using the front tracking version of the method with the same grid size.

a) $\psi = 0$ level sets



b) Tracked interfaces

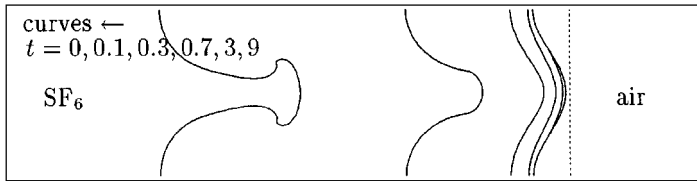


FIG. 13. A comparison plot of the interface locations for the Richtmyer–Meshkov instability, a Mach 1.24 shock wave in air, and an air-SF₆ interface case. (a) Results using the high-resolution wave propagation method with interfaces represented by $\psi = 0$ level sets. (b) Results using the front tracking version of the high-resolution wave propagation method. Interface locations are shown at six different times. The dashed line in each figure is the initial shock location which is captured in this case.

convergence behavior of the density profile under mesh refinement, and in particular the pressure, is free of spurious oscillations near the interface.

EXAMPLE 6.2. We now consider an air-liquid interface that is interacting with a planar Mach 1.95 shock wave in liquid. We use the same initial data as in Example 4.3 with the interface represented by (28) in the current case. We carry out various tests as were done in the previous example, and obtain the results shown in Figs. 15–18. The complex wave structure is once again present in this problem, and is very well computed when using the algorithm. Notice that for this problem the phase of the interface has shifted

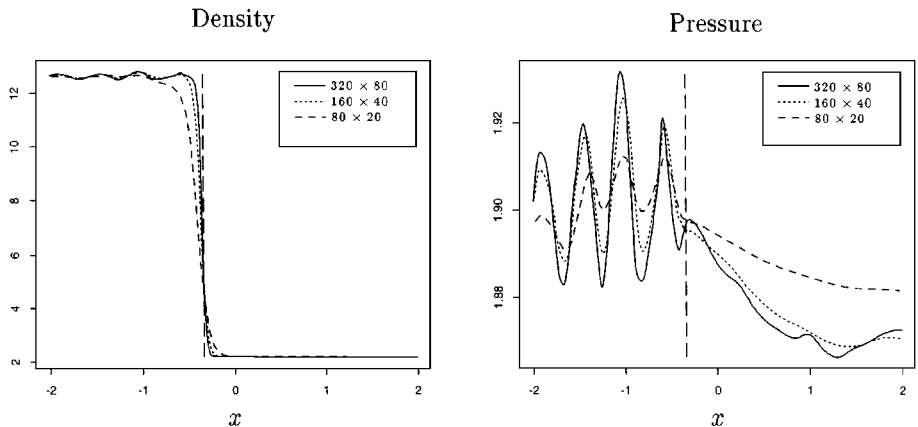


FIG. 14. A convergence study of the density and pressure for the Richtmyer–Meshkov instability, a Mach 1.24 shock wave in air, and an air-SF₆ interface case. The test is performed using three different grid systems, and the solutions are plotted along line $y = 0.5$ at time $t = 9$. The vertical dashed line in the figure is the interface location obtained using the front tracking method.

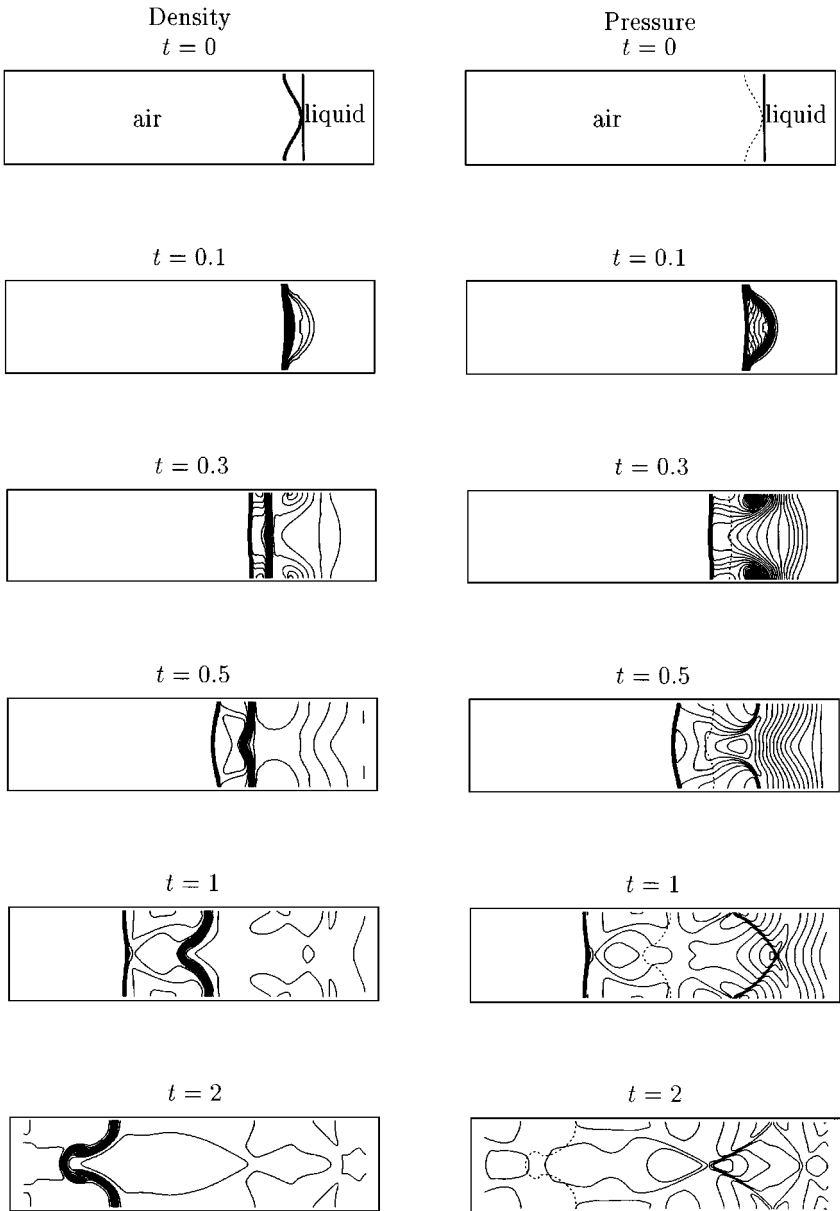


FIG. 15. Results for the simulation of Richtmyer–Meshkov instability, a Mach 1.95 shock wave in liquid, and an air–liquid interface case. The density and pressure contours (in logarithmic scale) are shown at six different times obtained using the high-resolution wave propagation method with a 320×80 grid. The dashed line in the pressure contour plot is the $\psi = 0$ level set introduced in the simulation as a passive quantity for representing the approximate location of the interface.

over 180 degrees. This interface behavior is commonly seen when the shock wave is propagating from the heavy fluid to the interface that has the light fluid on the other side (cf. [32, 75]).

We note that as far as the global wave structure is concerned the results presented here are reasonable ones as compared to those appearing in the literature [11, 32]. A more careful study of the solutions that covers results from the theoretical prediction of a nonlinear theory

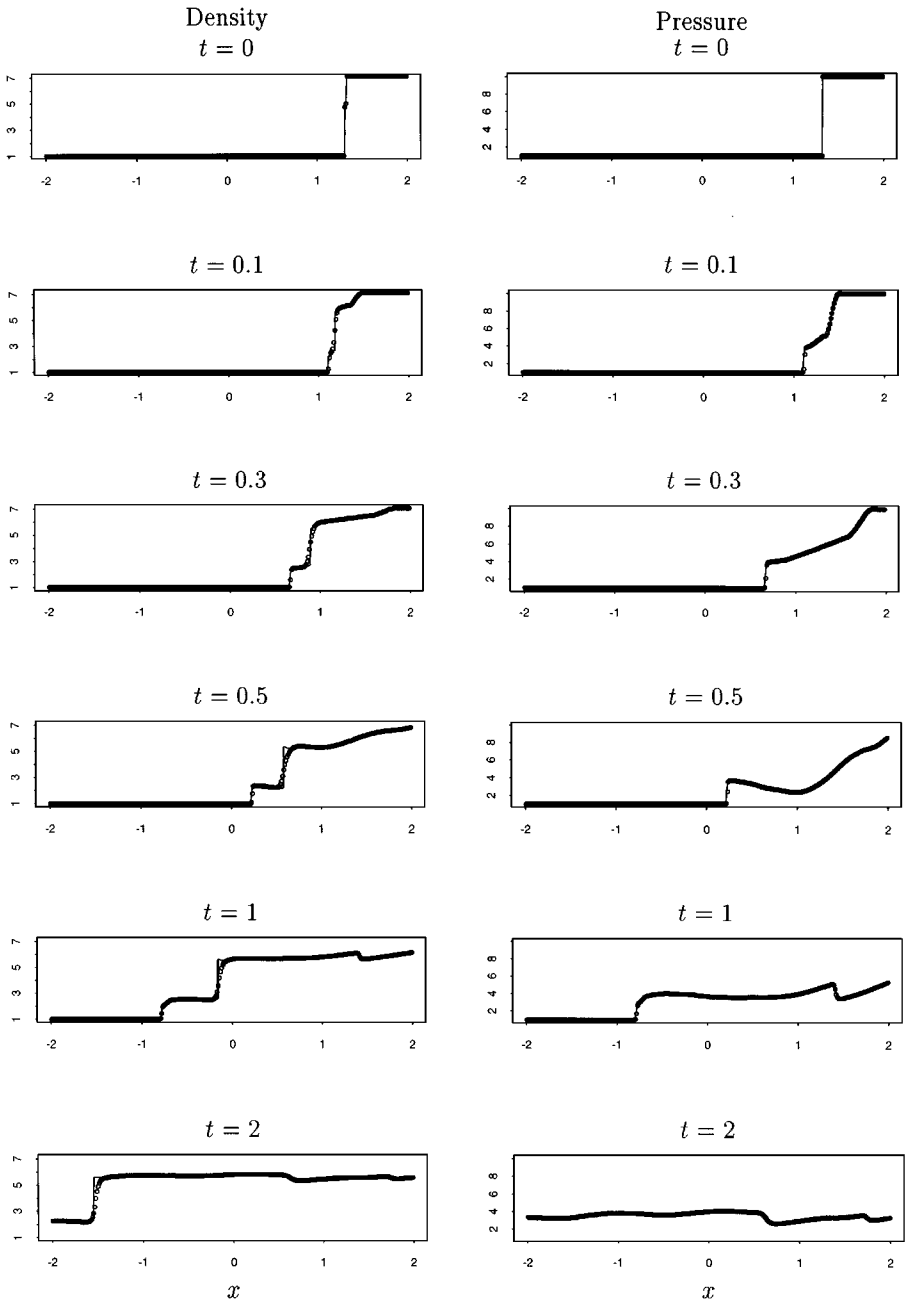
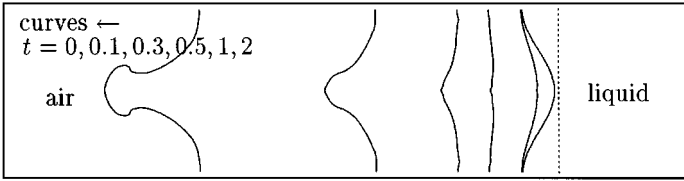


FIG. 16. The cross-sectional plots of the results for the run shown in Fig. 15 along line $y = 0.5$, where the solid lines are results obtained using the front tracking version of the method with the same grid size.

developed by Zhang and Sohn [76] and the laboratory experiments [27, 73] will be reported elsewhere [66].

7. CONCLUSIONS

The generalization of shock-capturing methods originally designed for single-component flows to the case of a multicomponent flow requires some thoughts. The principle problem

a) $\psi = 0$ level sets

b) Tracked interfaces

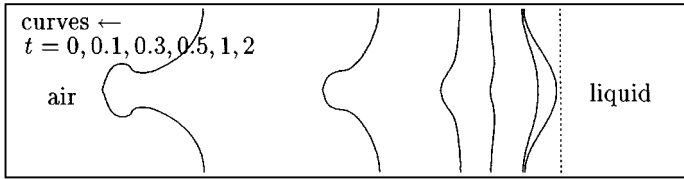


FIG. 17. A comparison plot of the interface locations for the Richtmyer–Meshkov instability, a Mach 1.95 shock wave in liquid, and an air–liquid interface case. (a) Results using the high-resolution shock-capturing method with interfaces represented by $\psi = 0$ level sets. (b) Results using the high-resolution front tracking method. Interfaces are shown at six different times. The dashed line in each figure is the initial shock location which is captured in this case.

in the usual extension is the occurrence of spurious pressure oscillations when two or more fluid components are present in a grid cell. Here we consider a compressible flow problem with a stiffened gas equation of state as an example. We show that by choosing the correct set of model equations (i.e., the quasi-conservative formulation of the γ -based and volume-fraction models) accurate results can be obtained using standard methods for a single-component flow. Here we have employed the high-resolution wave propagation method with the Roe solver for the computations, giving an efficient implementation of the algorithm. Validation of our multicomponent approach is clearly established by test results present in the paper.

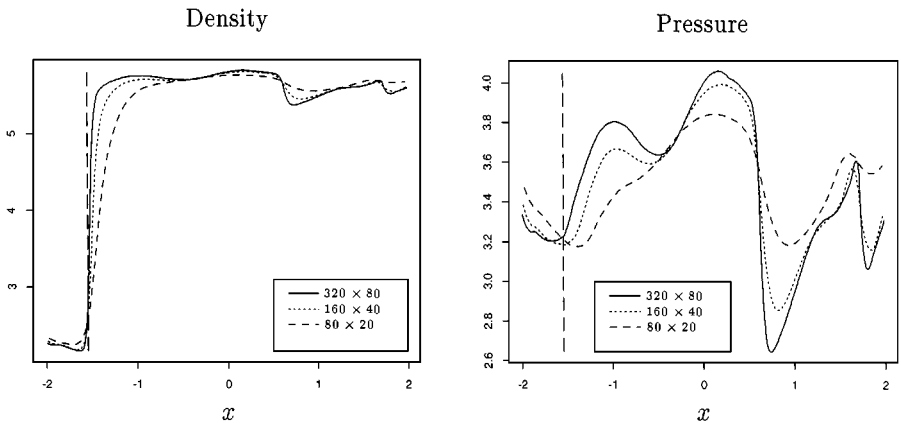


FIG. 18. A convergence study of the interface locations for the Richtmyer–Meshkov instability, a Mach 1.95 shock wave in liquid, and an air–liquid interface case. The test is performed using three different grid systems, and the solutions are plotted along line $y = 0.5$ at time $t = 2$. The vertical dashed line in the figure is the interface location obtained using the front tracking method.

Ongoing work is to further test the approach for realistic problems with interfaces separating regions of low and high Mach number flows and with very stiff equation of states. Model examples to be considered are the popular water-drop problems in air and the rising air bubble problems in water [8, 69], but now in a compressible flow environment. Extension of the method to a Mie–Grüneisen type equation of state of condensed materials [50, 51], to real gases [15, 48, 62], and to reacting flows [6, 10, 16, 30] will be looked at. Realization of the algorithm that couples with front tracking and adaptive mesh refinement [3–5] will be considered in the future also.

ACKNOWLEDGMENTS

This work was supported in part by National Science Council of Republic of China Grants NSC-84-2121-M-002-023 and NSC-86-2115-M-002-005. The author thanks the anonymous reviewers for useful comments that helped to improve the first draft of the manuscript.

REFERENCES

1. R. Abgrall, How to prevent pressure oscillations in multicomponent flow calculations: A quasi conservative approach, *J. Comput. Phys.* **125**, 150 (1996).
2. M. Arora and P. L. Roe, A well-behaved TVD limiter for high-resolution calculations of unsteady flow, *J. Comput. Phys.* **132**, 3 (1997).
3. J. B. Bell, M. Berger, J. Saltzman, and M. Welcome, Three-dimensional adaptive mesh refinement for hyperbolic conservation laws, *SIAM J. Sci. Comput.* **15**(1), 127 (1994).
4. J. B. Bell, P. Colella, and M. L. Welcome, Conservative front-tracking for inviscid compressible flow, UCRL-JC-105251, preprint, 1991.
5. M. J. Berger and P. Colella, Local adaptive mesh refinement for shock hydrodynamics, *J. Comput. Phys.* **82**, 64 (1989).
6. A. Bourlioux and A. J. Majda, Theoretical and numerical structure of unstable detonations, *Philos. Trans. R. Soc. London A* **350**, 29 (1995).
7. T. Chang and L. Hsiao, *The Riemann Problem and Interaction of Waves in Gas Dynamics* (Longman, England, 1989).
8. Y. C. Chang, T. Y. Hou, B. Merriman, and S. Osher, A level set formulation of Eulerian interface capturing methods for incompressible fluid flows, *J. Comput. Phys.* **124**, 449 (1996).
9. D. Chargy, R. Abgrall, L. Fezoui, and B. Larroutrou, *Comparisons of Several Upwind Schemes for Multi-component One-Dimensional Inviscid Flows*, INRIA Rep. 1253, 1990.
10. J. F. Clark, S. Karni, J. J. Quirk, P. L. Roe, L. G. Simmonds, and E. F. Toro, Numerical computation of two-dimensional unsteady detonation waves in high energy solids, *J. Comput. Phys.* **106**, 215 (1993).
11. L. D. Cloutman and M. F. Wehner, Numerical simulation of Richtmyer–Meshkov instabilities, *Phys. Fluids A* **4**, 1821 (1992).
12. J. P. Cocchi, R. Saurel, and J. C. Loraud, Treatment of interface problems with Godunov-type scheme, *Shock Waves* **5**, 347 (1996).
13. P. Colella, A direct Eulerian MUSCL scheme for gas dynamics, *SIAM J. Sci. Stat. Comput.* **6**, 104 (1985).
14. P. Colella, R. E. Ferguson, and H. M. Glaz, Multifluid algorithms for Eulerian finite difference methods, in preparation.
15. P. Colella and H. M. Glaz, Efficient solution algorithms for the Riemann problem for real gases, *J. Comput. Phys.* **59**, 264 (1985).
16. P. Colella, A. Majda, and V. Roytburd, Theoretical and numerical structure for reacting shock waves, *SIAM J. Sci. Stat. Comput.* **7**(4), 1059 (1986).
17. C. H. Cooke and T.-J. Chen, Continuous front tracking with subcell resolution, *J. Sci. Comput.* **6**, 269 (1991).
18. R. Courant and K. O. Friedrichs, *Supersonic Flow and Shock Waves* (Wiley–Interscience, New York, 1948).

19. S. F. Davis, An interface tracking method for hyperbolic systems of conservation laws, *Appl. Numer. Math.* **10**, 447 (1992).
20. B. Einfeldt, C. D. Munz, P. L. Roe, and B. Sjogreen, On Godunov type methods near low densities, *J. Comput. Phys.* **92**, 273 (1991).
21. R. P. Fedkiw, X.-D. Liu, and S. Osher, *A General Technique for Eliminating Spurious Oscillations in Conservative Schemes for Multiphase and Multispecies Euler Equations*, UCLA, CAM Rep. 97-27, 1997.
22. C. L. Gardner, J. Glimm, O. McBryan, R. Menikoff, D. H. Sharp, and Q. Zhang, The dynamics of bubble growth for Rayleigh–Taylor unstable interfaces, *Phys. Fluids* **31**, 447 (1988).
23. P. Glaister, An approximate linearised Riemann solver for the Euler equations for real gases, *J. Comput. Phys.* **74**, 382 (1988).
24. P. Glaister, An efficient algorithm for compressible flows with real gases, *Int. J. Numer. Methods Fluids* **9**, 1269 (1989).
25. J. Glimm, J. Grove, X. L. Li, K.-M. Shyue, Y. Zeng, and Q. Zhang, Three dimensional front tracking, *SIAM J. Sci. Comput.*, in press.
26. E. Godlewski and P.-A. Raviart, *Numerical Approximation of Hyperbolic Systems of Conservation Laws*, Applied Mathematical Science (Springer-Verlag, New York/Berlin, 1996), Vol. 118.
27. J. Grove, R. Holmes, D. H. Sharp, Y. Yang, and Q. Zhang, Quantitative theory of Richtmyer–Meshkov instability, *Phys. Rev. Lett.* **7121**, 3473 (1993).
28. J. Grove and R. Menikoff, The anomalous reflection of a shock wave at a material interface, *J. Fluid Mech.* **219**, 313 (1990).
29. F. Harlow and A. A. Amsden, *Fluid Dynamics*, Monograph LA-4700, Los Alamos National Laboratory, Los Alamos, NM, 1971.
30. J. Hilditch and P. Colella, A front tracking method for compressible flame in one dimension, *SIAM J. Sci. Comput.* **16**(4), 755 (1995).
31. K. S. Holian, *T-4 Handbook of Material Properties Data Bases*, Tech. Rep. LA-10160-MS, Los Alamos National Laboratory, Los Alamos, NM, 1984.
32. R. L. Holmes, *A Numerical Investigation of the Richtmyer–Meshkov Instability Using Front Tracking*, Ph.D. thesis, SUNY at Stony Brook, August, 1994 (unpublished).
33. P. Jenny, B. Mueller, and H. Thomann, Correction of conservative Euler solvers for gas mixtures, *J. Comput. Phys.* **132**, 91 (1997).
34. S. Karni, Multicomponent flow calculations by a consistent primitive algorithm, *J. Comput. Phys.* **112**, 31 (1994).
35. S. Karni, Hybrid multifluid algorithms, *SIAM J. Sci. Comput.* **17**, 1019 (1996).
36. S. Karni, A level-set capturing scheme for compressible interfaces, submitted for publication.
37. J. O. Langseth and R. J. LeVeque, A wave propagation method for three-dimensional hyperbolic conservation laws, submitted for publication.
38. B. Larroutourou, How to preserve the mass fractions positivity when computing compressible multi-component flows, *J. Comput. Phys.* **95**, 59 (1991).
39. B. Larroutourou and L. Fezoui, On the equations of multi-component perfect or real gas inviscid flow, in *Nonlinear Hyperbolic Problems*, edited by C. Carasso, P. Charrier, B. Hanouzet, and J.-L. Joly, Lect. Notes in Math. (Springer-Verlag, New York/Berlin, 1989), Vol. 1402.
40. R. J. LeVeque, High resolution finite volume methods on arbitrary grids via wave propagation, *J. Comput. Phys.* **78**, 36 (1988).
41. R. J. LeVeque, Hyperbolic conservation laws and numerical methods, in *Von Karman Institute for Fluid Dynamics, 1990*, Lecture Series on Computational Fluid Dynamics, 1990-03.
42. R. J. LeVeque, *Numerical Methods for Conservation Laws* (Birkhäuser-Verlag, Basel, 1992), 2nd ed.
43. R. J. LeVeque, Wave propagation algorithms for multi-dimensional hyperbolic systems, *J. Comput. Phys.* **131**, 327 (1997).
44. R. J. LeVeque and K.-M. Shyue, One-dimensional front tracking based on high resolution wave propagation methods, *SIAM J. Sci. Comput.* **16**, 348 (1995).

45. R. J. LeVeque and K.-M. Shyue, Two-dimensional front tracking based on high resolution wave propagation methods, *J. Comput. Phys.* **123**, 354 (1996).
46. R. L. LeVeque, CLAWPACK, available from netlib.att.com in netlib/pdes/claw or on the Web at the URL <http://www.amath.washington.edu/rjl/clawpack.html>.
47. R. L. LeVeque, CLAWPACK: A software package for solving multi-dimensional conservation laws, in *Proc. 5th Intl. Conf. Hyperbolic Problems* (World Scientific, Singapore, 1996), pp. 188–197.
48. M.-S. Liou, B. van Leer, and J.-S. Shuen, Splitting of inviscid fluxes for real gases, *J. Comput. Phys.* **87**, 1 (1990).
49. S. P. Marsh, *LASL Shock Hugoniot Data* (Univ. California Press, Berkeley, 1980).
50. R. Menikoff and B. Plohr, The Riemann problem for fluid flow of real materials, *Rev. Mod. Phys.* **61**, 75 (1989).
51. G. H. Miller and E. G. Puckett, A high order Godunov method for multiple condensed phases, *J. Comput. Phys.* **128**, 134 (1996).
52. W. Mulder, S. Osher, and J. A. Sethian, Computing interface motion in compressible gas dynamics, *J. Comput. Phys.* **100**, 209 (1992).
53. S. Osher and J. A. Sethian, Fronts propagating with curvature-dependent speed: Algorithm based on Hamilton–Jacobi formulations, *J. Comput. Phys.* **79**, 12 (1988).
54. B. J. Plohr, Shockless acceleration of thin plates modeled by a tracked random choice method, *AIAA J.* **26**(4), 470 (1988).
55. E. G. Puckett and J. S. Saltzman, A 3D adaptive mesh refinement algorithm for multimaterial gas dynamics, *Phys. D* **60**, 84 (1992).
56. J. J. Quirk, A contribution to the great Riemann solver debate, *Int. J. Numer. Methods Fluids* **18**, 555 (1994).
57. R. D. Richtmyer, Taylor instability in shock acceleration of compressible fluids, *Comm. Pure Appl. Math.* **13**, 297 (1960).
58. P. L. Roe, Approximate Riemann solvers, parameter vector, and difference scheme, *J. Comput. Phys.* **43**, 357 (1981).
59. P. L. Roe, Fluctuations and signals—A framework for numerical evolution problems, in *Numerical Methods for Fluid Dynamics*, edited by K. W. Morton and M. J. Baines (Academic Press, San Diego, 1982), pp. 219–257.
60. P. L. Roe, Upwind schemes using various formulations of the Euler equations, in *Numerical Methods for the Euler Equations of Fluid Dynamics*, edited by F. Angrand, A. Dervieux, J. A. Desideri, and R. Glowinski (SIAM, Philadelphia, 1985), pp. 14–31.
61. R. Samtaney, *Vorticity in Shock-Accelerated Density-Stratified Interfaces: An Analytical and Computational Study*, Ph.D. thesis, Rutgers, State University of New Jersey, October 1993 (unpublished).
62. R. Saurel, M. Larini, and J. C. Loraud, Exact and approximate Riemann solvers for real gases, *J. Comput. Phys.* **112**, 126 (1994).
63. J. A. Sethian, *Level Set Methods: Evolving Interfaces in Geometry, Fluid Mechanics, Computer Vision, and Material Science* (Cambridge Univ. Press, Cambridge, UK, 1996).
64. D. H. Sharp, An overview of Rayleigh–Taylor instability, *Phys. D* **12**, 3 (1984).
65. K.-M. Shyue, *Efficient High-Resolution Wave Propagation Methods for Computing Inviscid Compressible Flow with Interfaces*, Final Report, NSC84-2121-M-002-023, National Science Council, Taiwan, R.O.C., 1995 (unpublished).
66. K.-M. Shyue, A front tracking method applied to compressible unstable interface problems, in preparation.
67. K.-M. Shyue, Godunov-type shock capturing methods for multicomponent problems with van der Waals fluids, in preparation.
68. J. Smoller, *Shock Waves and Reaction-Diffusion Equations* (Springer-Verlag, New York, 1982).
69. M. Sussman, P. Smereka, and S. Osher, A level set method for computing solutions to incompressible two-phase flow, *J. Comput. Phys.* **114**, 146 (1994).
70. P. K. Sweby, High resolution schemes using flux limiters for hyperbolic conservation laws, *SIAM J. Numer. Anal.* **21**, 995 (1984).

71. V. Ton, Improved shock-capturing methods for multicomponent and reacting flows, *J. Comput. Phys.* **128**, 237 (1996).
72. B. van Leer, Towards the ultimate conservative difference scheme. V. A second order sequel to Godunov's method, *J. Comput. Phys.* **32**, 101 (1979).
73. M. Vetter and B. Sturtevant, Experiments on Richtmyer–Meshkov instability of an air/SF₆ interface, *Shock Waves* **4**, 247 (1995).
74. K. Xu, BGK-based scheme for multicomponent flow calculations, *J. Comput. Phys.* **134**, 122 (1997).
75. Y. Yang, Q. Zhang, and D. H. Sharp, Small amplitude theory of Richtmyer–Meshkov instability, *Phys. Fluids* **6**(5), 1856 (1994).
76. Q. Zhang and S.-I. Sohn, An analytical nonlinear theory of Richtmyer–Meshkov instability, *Phys. Lett. A* **212**, 149 (1996).